Wireless Power Transfer for Switcher Trains

NCDOT Project 2020-40
FHWA/NC/2020-40
June 2023

Tiefu Zhao, Ph.D., et. al
Associate Professor
Electrical and Computer Engineering
University of North Carolina at Charlotte

UNIVERSITY OF NORTH CAROLINA
CHARLOTTE

RESEARCH & DEVELOPMENT

1. Report No. **FHWA/NC/2020-40**	2. Government Accession No.	3. Recipient's Catalog No.	
4. Title and Subtitle Wireless Power Transfer for Switcher Trains		5. Report Date June 2023	
		6. Performing Organization Code	
7. Author(s): Tiefu Zhao, Ph.D., Shenen Chen, Ph.D., Nicole Braxtan, Ph.D.		8. Performing Organization Report No.	
9. Performing Organization Name and Address University of North Carolina at Charlotte The William States Lee College of Engineering 9201 University City Blvd., Charlotte, NC 28223-0001		10. Work Unit No. (TRAIS)	
		11. Contract or Grant No. FHWA/NC/2020-40	
12. Sponsoring Agency Name and Address North Carolina Department of Transportation Research and Development Unit 1020 Birch Ridge Drive, Building B Raleigh, NC 27610		13. Type of Report and Period Covered Final Report August 1, 2019 – December 31, 2022	
		14. Sponsoring Agency Code NCDOT Project # 2020-40	

Supplementary Notes:

16. Abstract

   To address the issue of charging off-road switcher equipment at railroad yards, UNC Charlotte team is first in the nation to develop this one-of-a-kind wireless power technology for rail application. A wireless power charging system for switcher trains at the North Carolina DOT Rail Yard is developed in this project. The system would allow the switcher trains to be charged overnight and minimize the heavy labor involved in the current plug-in charging system – thus minimizing exposing rail yard personnel to working hazards due to heavy loading. The proposed wireless charging system will provide substantial support for the rapid and reliable charging of the electric power supply of the switcher trains, which will greatly facilitate NCDOT's asset management in terms of efficiency, effectiveness, and safety. Ultimately, the results of this research will also benefit NCDOT with respect to the enhancement of the safety of yard operations, minimizing environmental impacts, increasing worker safety, and reducing pollution.
   The key innovations developed in the project include novel W-I magnetic couple design and power electronic converters, achieving highest efficiency reported for railway application. The project supports students' academic progress by providing them hands-on, real-world, experiential learning opportunities. The project also helps forge strong partnerships for technology innovation and demonstration between UNC Charlotte and our local communities - Belmont Trolley and the City of Belmont. The project was highlighted by PBS Charlotte TV in the episode "TRAIL OF HISTORY: Historic Infrastructure" in Mar 2023.

17. Key Words Wireless power transfer, battery charging, rail application, safety, efficiency	18. Distribution Statement		
19. Security Classif. (of this report) Unclassified	20. Security Classif. (of this page) Unclassified	21. No. of Pages 61	22. Price

Form DOT F 1700.7 (8-72)   **Reproduction of completed page authorized**

Executive Summary:

To address the issue of charging off-road switcher equipment at railroad yards, a wireless power charging system for switcher trains at the North Carolina DOT Rail Yard is being developed. The system would allow the switcher trains to be charged overnight and minimize the heavy labor involved in the current plug-in charging system – thus minimizing exposing rail yard personnel to working hazards due to heavy loading. Based on the principle of inductive power transfer (IPT), wireless power charging system minimizes the use of power cords and can eliminate several potential safety issues associated with power cords. IPT is a novel technology that has seen significant use in electric vehicle (EV) applications. However, the technology development for tracked locomotives is very limited. Multiple prototypes of different power scales have been developed throughout this project with a final design using a modular W-I coupler system. The proposed wireless charging system will provide substantial support for the rapid and reliable charging of the electric power supply of the switcher trains, which will greatly facilitate NCDOT's asset management in terms of efficiency, effectiveness, and safety. Ultimately, the results of this research will also benefit NCDOT with respect to the enhancement of the safety of yard operations.

Our major findings are summarized below:

1) A detailed state-of-the-art rail wireless power has been technology review was performed showing different available wireless power charging designs.
2) A sub-scale system has been developed to demonstrate the effectiveness of wireless power charging including the effects of increased air gap (vertical separation) and horizontal shifts.
3) A full-scale, W-I shape coupler-based IPT system has been developed for wirelessly charging rail locomotive batteries. The W-I shaped coupler has a relatively higher coupling coefficient and a significantly lower core volume, which can reduce the core material cost and maintain high power transfer capability. Its modular design is easy to extend to achieve a higher power rating and is competent for both static and dynamic charging.
4) The full-scale, modular W-I shape coupler-based IPT system was constructed and validated at **5 kW with 92.5% efficiency**, which is **the highest IPT system efficiency reported for railway applications**.
5) The electromagnetic field (EMF) was also measured at different test points according to the standards to ensure the safety of the designed wireless charging system.
6) All studies have been validated using numerical models developed using ANSYS Maxwell.
7) The full-scale prototype was **demonstrated** in a full-scale trailer cart from **Belmont Trolley** Co. on October 12, 2022.
8) A separate IPT system using thin copper sheets and 4-turn receiver coil (by RPS) was also presented as an alternative design that is currently being customized for full-scale implementations.

Appendix: Table of Contents

List of Figures

List of Tables

Acknowledgments

List of Acronyms

3D	Three dimensional
A	Ampere
AC	Alternating Current
ADC	Analog to Digital Converter
APT	Acoustic Power Transfer
CO2	Carbon Dioxide
CPT	Capacitive Power Transfer
DC	Direct Current
DSP	Digital Signal Processor
EMF	Electromagnetic Field
EMI	Electromagnetic Interference
ESR	Equivalent Series Resistance
EV	Electric Vehicle
FEA	Finite Element Analysis
HF	High-Frequency
ICNIRP	International Commission on Non-Ionizing Radiation Protection
IPT	Inductive Power Transfer
ISE	Fraunhofer Institute for Solar Energy Systems
J	Joule
KAIST	Korea Advanced Institute for Science and Technology
kW	Kilowatt
MMF	Magnetomotive Force
MPPT	Maximum Power Point Tracking
MPT	Microwave Power Transfer
ms	Millisecond
MW	Megawatt (Unit)
nF	Nano Farad
OPT	Optical Power Transfer
ORNL	Oak Ridge National Laboratory
PCB	Printed Circuit Board
RF	Radio Frequency
RMS	Root Mean Square
Rx	Receiver
s	Second
SiC	Silicon Carbide
T	Tesla
Tx	Transmitter
V	Volt
VA	Volt-Amp
WPT	Wireless Power Transfer
ZPA	Zero Phase Angle
ZVS	Zero Voltage Switching
μH	Microhenry

1. Introduction

1.1. Background

The North Carolina Department of Transportation (NCDOT) Rail Division currently owns a fleet of eight (8) F59PH and PHI diesel-electric locomotives that are used in its Piedmont passenger rail service between Raleigh and Charlotte, NC. When not in operation these locomotives are plugged into electrical ground power – 480V/400A three-phase – to keep their batteries charged and provide power to all onboard systems on a passenger car (lights, HVAC, etc.) in the yard, which is a standard industry practice. Figure 1.1 shows the wired power charging at the wayside of the locomotive. The plug-in procedure requires parking the vehicles at specific locations and the physical attachment of a heavy cable adaptor to the locomotive (Figure 1b). The physical attachment of the wired adaptors has the potential of causing back pain, tripping personnel working on the tracks, and other labor safety-related risks. The physical attachment process is also tedious and requires time to secure the adaptor to the train battery. Furthermore, the tears and wears of the physical cable adaptors can be a nuisance cost item for the DOT in the long run.

(a) (b)
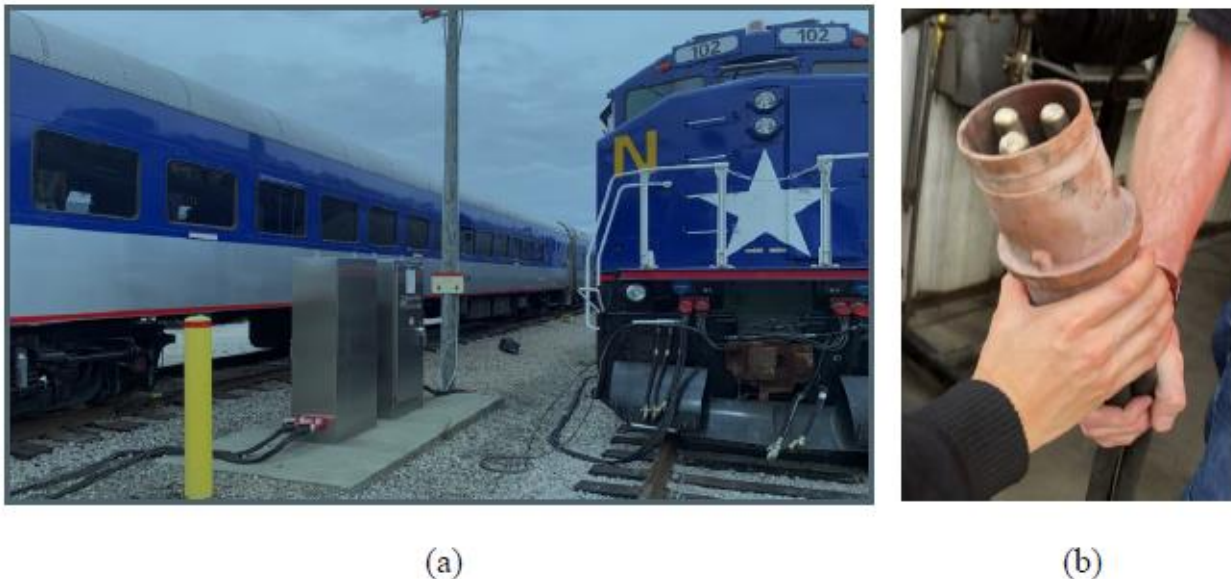
Figure 1.1 Current Power Charging of a Locomotive with Standard Plug-In Power Lines: (a) A charging locomotive and its charging station; (b) Heavy electrical cable and terminal for charging the locomotives

The power cords shown in Figure 1.1 (b), which are bulky and heavy, have to be moved from the power station to the railway and manually connected to the locomotive. The staff responsible for charging the locomotives is exposed to the risk of electric shock and arc flash while disconnecting cables when the circuit is live.

Alternatively, the diesel-electric locomotive battery charging can be accomplished via wireless power transfer (WPT) technologies - By equipping the locomotive with an electrical receiver and parking it over an electrical charging mat embedded under the rail, the wireless power transfer setup can completely remove the physical labor involved in the power connection. The charging infrastructure and the onboard system are wirelessly connected via magnetic coupling. The coupled systems have the feature of galvanic isolation, which reduces electrical shock and safety risk. Furthermore, by getting rid of the

components associated with the cables, the WPT system on locomotives is more flexible and reliable and with better resistance against adverse weather conditions. Different from the wireless power charging technology on roadway applications, the rail tracks provide the locomotives with a fixed route, thus eliminating the lateral misalignment problem, which is very common in EV WPT charging systems. Finally, other than increased worker safety, the implementation of a WPT charging station would also afford time savings for workers and would be a technological step forward for the rail industry.

While there are several WPT technologies available, the most commonly used for vehicles is the Inductive Power Transfer (IPT) technology: Figure 1.2 depicts a conceptual IPT system for charging a train wirelessly [1]. The IPT system for the railway application contains a transmitter infrastructure embedded between the tracks and an on-board receiver system located on the underbelly of the locomotive. The DC (direct current) power is converted to a high-frequency AC (alternate current) power and injected into the transmitter coil via an inverter. The power is transferred wirelessly via the coupled coils with a certain airgap distance. During this procedure, energy was transduced from electrical energy to magnetic energy in the transmitter and then transduced back to electrical energy in the receiver. Aimed to reduce the (volt-ampere) VA rating as well as maximize the power transfer capability, the compensation circuits on the transmitter and receiver sides are resonant with the transmitter and receiver coils, respectively. The high-frequency induced voltage on the receiver side is then converted to a DC voltage by a rectifier. A DC/DC converter might be used to control the power flow from the receiver to the batteries and loads. Therefore, the IPT design needs to consider both magnetic design (coupler) and electrical design (compensation circuits and converters).
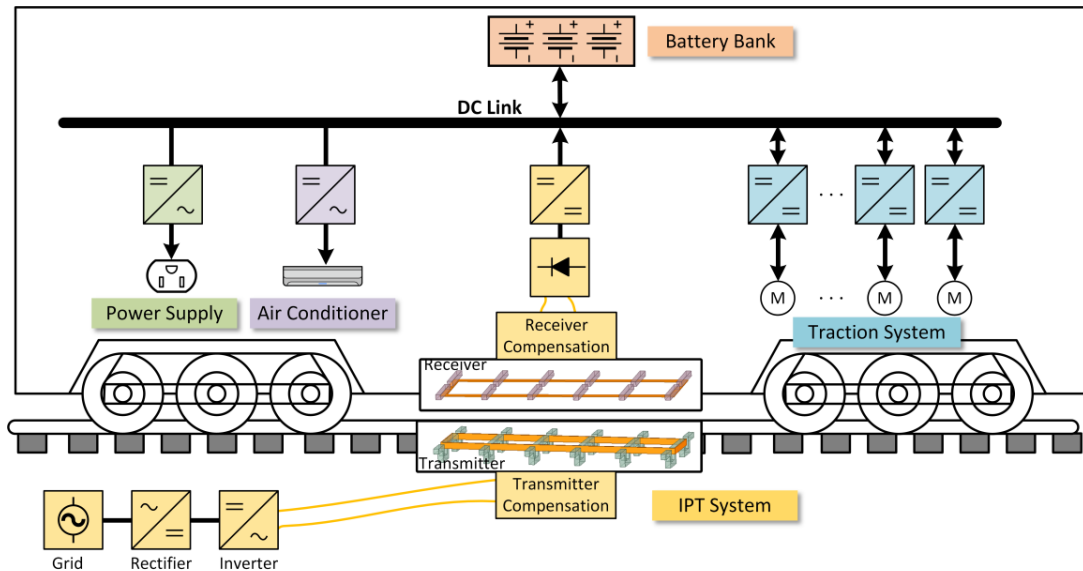
Figure 1.2 Conceptual diagram of wireless train charging application [1]

1.2. Research Need Definition

The proposed WPT charging system at the NCDOT Rail Yard is a state-of-the-art inductive power transfer (IPT) technology which transfers power from the transmitter (on track) to the receiver (on locomotive) based on the principle of electromagnetic induction over an air gap. Due to this contactless transmission, IPT is the preferable WPT technology for transportation application with benefits including, but not limit to, power transmission in intricate geographical environments and during severe weather conditions. Moreover, by improving the power rating and efficiency, which used to be the shortcomings from loose coupling, the IPT technology shows a strong potential to reform the future railway industry [2], especially for substitution of traditional diesel-fueled locomotives.

While IPT technology has matured for electric vehicles and microelectronic systems such as cell phone and laptop computers, the biggest challenges for the proposed WPT system for rail yard applications, however, are associated with the high voltage power supply and the physical placement of the electromagnetic coils for both receivers and transmitter (typically between the railroad tracks) [3, 4]. As a result, additional studies are needed to investigate the process of physical placement of the electromagnetic coils between metallic components including railroad tracks and locomotives, which requires innovative designs to eliminate the physical challenges including influences on the electromagnetic fields of the coils.

1.3. Research Objectives

In this study, the wireless power transfer (WPT) technology has been investigated and developed for rail applications. The concept was first proposed by Nicola Tesla at the turn of the 20th century [5], however, the development of WPT technology was very slow until the end of the 20th century because of the limitations in power electronics. Figure 1.3 depicts the classification of WPT technology by the category of field, which includes acoustic power transfer (APT), optical power transfer (OPT), microwave power transfer (MPT), inductive power transfer (IPT), and capacitive power transfer (CPT) [6].

For the railroad application, three objectives are to be accomplished:

1) Design and construction of a WPT prototype system including power converters and coil designs, and optimization of parameters for charging efficiencies such as static charging time, rate, and setup design.
2) Develop WPT coil placement and system safety design for the rail yard implementation.
3) Conduct field validation study at a rail facility to demonstrate field implementation.
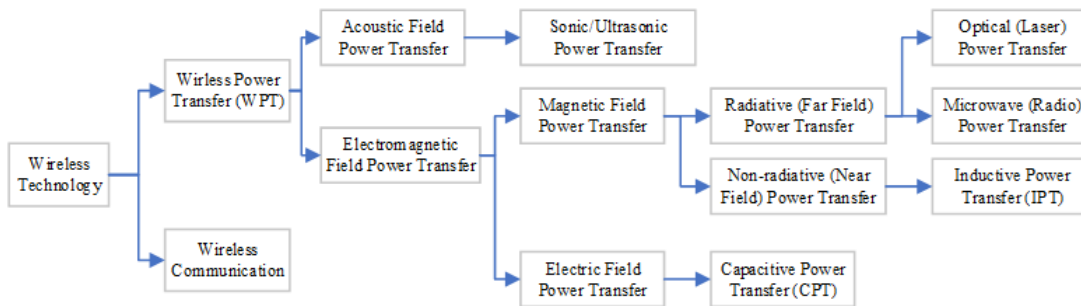
Figure 1.3 Classification of Wireless Power Charging Technologies. [6]

1.4. Report Organization

This report is organized in a manner that a comprehensive literature review on the wireless power charging technology and the issues associated with rail transportation applications are presented in Chapter 2, followed by a detailed description of the technology development methodologies in Chapter 3 and finally the conclusions in Chapter 4. In particular, a full-scale system demonstration was performed at the Belmont Trolley Public Works facility on October 12, 2022 – over 160 people were present at the demonstration. The event is summarized in Section 3.3. Specific recommendations regarding adoption strategies for NCDOT are included in Chapter 5 and future implementation and technology transfer plans in Chapter 6.

2. Literature Review

Since Nicola Tesla proposed the wireless power transfer concept, IPT technology has been investigated extensively. However, the development of IPT technology was very slow until the end of the 20th century because of the limitations in power electronics. With the emerging development of wide bandgap devices, IPT research is growing rapidly to achieve a higher power output and higher efficiency at a lower cost. During the past decades, numerous research institutes have proposed different IPT systems and demonstrated several prototypes for EV application. Witricity developed a 3.3 kW wireless charging system with an efficiency of 90% at 18 cm air gap in 2013 [7] and an 11kW wireless charging system with 91 – 94% efficiency in 2016 [8], respectively. IPT technology has presented a 100kW wireless charging solution for electric buses [9]. A team from the Fraunhofer Institute for Solar Energy Systems (ISE) demonstrated a 22kW bidirectional charging system with a pulse density modulation (PDM) method to achieve a system efficiency of 97.4% [10]. Oak Ridge National Laboratory (ORNL) proposed a 120kW IPT system with 96.9% DC-DC efficiency with a 5 inch (12.7 cm) air gap in 2018 [11]. Table 2-1 summaries some IPT system designs for EVs from industry and academia. IPT is shown to be a mature technology and is currently commercialized for EV applications.

Table 2-1 IPT system designs for EV applications

Name	Year	Air gap	Power	Efficiency	References
KAIST	2009	1 cm	3 kW	80%	[12]
KAIST	2009	17 cm	60 kW	72%	[13]
KAIST	2010	20 cm	15 kW/pick up	83%	[14]
KAIST	2010	20 cm	27 kW	80%	[15]
Bombardier	2013	N/A	200 kW	N/A	[16]
Witricity	2013	18 cm	3.7 kW	90%	[7]
Toshiba	2014	16 cm	7 kW	N/A	[17]
BOSCH	2015	N/A	7 kW	86%	[18]
Fraunhofer ISE	2015	13 cm	22 kW	97.40%	[10]
Witricity	2016	9 – 28 cm	11 kW	91 - 93%	[8]
INTIS	2016	11 cm	30 kW	N/A	[19]
ETH	2016	16 cm	50 kW	95.80%	[20]
Toshiba	2017	10 cm	44 kW	N/A	[21]
ORNL	2018	15 cm	50 kW	95%	[22]
ORNL	2018	12.7 cm	120 kW	96.90%	[11]
WAVE	2019	N/A	500 kW	N/A	[23]
Zhejiang University	2020	16 cm	50 kW	95.20%	[24]
Momentum dynamics	2021	N/A	450 kW	N/A	[25]
ORNL	2021		200 kW	98.30%	[26]
IPT technology	N/A	N/A	100 kW	N/A	[9]

2.1. Wireless Power Transfer Technology

Inductive power transfer (IPT) is typically described as a loosely coupled coil set and is theorized using both Ampere's law and Faraday's law, where a time-varying current (alternative current) flows through the primary coil that generates a time-varying magnetic flux (Ampere's law). When the secondary coil is in close vicinity to the primary coil, the time-varying magnetic flux induces a magnetic flux, which in turn, generates a current in the secondary coil (Faraday's law). The differential forms of Ampere's and Faraday's laws are presented as:

$$\nabla \times H = J + \frac{\partial D}{\partial t} \tag{2.1}$$

and

$$\nabla \times E = -\frac{\partial B}{\partial t} \tag{2.2}$$

where H and E are the vector magnetic field intensity and electric field intensity, respectively. The magnetic flux density and the electric flux density are represented by B and D, respectively. And finally, the current density is represented by J.

IPT coils are in essence inductors whose magnetic flux links with each other when they are in each other's vicinity. The self-inductance of a magnetic structure is defined as the ratio of total flux linkage to the current that generates the flux:

$$L_{self} = \frac{N\phi}{I} \tag{2.3}$$

where I is the excitation current generating the flux, Φ is the total flux generated by the coil, and N represents the number of turns in the structure.

Since Φ is directly proportional to the number of turns, N, in the magnetic coil, L_{self} is also proportional to N. The mutual flux linkage between the two coil is described using the coupling coefficient, $k_{12,}$

$$k_{12} = \frac{M_{12}}{\sqrt{L_1 L_2}} \tag{2.4}$$

where M_{12} is the mutual inductance and L_1 and L_2 are the self-inductances of the primary and secondary coils, respectively. Figure 2.1 shows the two loosely coupled coils where the voltages, v_1, v_2 and currents, i_1, i_2 of each coil are represented as:

$$v_1 = L_1 \frac{di_1}{dt} + M_{12} \frac{di_2}{dt} \tag{2.5}$$

$$v_2 = L_2 \frac{di_2}{dt} + M_{12} \frac{di_1}{dt} \tag{2.6}$$
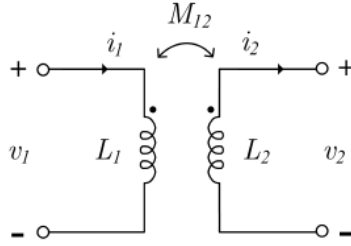
Figure 2.1 Circuit diagram of two loosely coupled coils showing a single transmitter and a single receiver

Assuming L_s and L_p are the self-inductance of the transmitter coil and receiver coil with a mutual inductance M and the track current (current in transmitter coil) I_1 operating at an angular frequency ω, the induced voltage on the receiver is then [27],

$$V_{oc} = j\omega M I_1 \tag{2.7}$$

If the receiver side is shorted, then the short current is,

$$I_{sc} = \frac{V_{oc}}{j\omega L_p} = \frac{M I_1}{L_p} \tag{2.8}$$

The product of (2.7) and (2.8) is the maximum VA rating for the receiver, P_{su}. The maximum power P_{out} that the system can transfer is then,

$$P_{out} = P_{su} \cdot Q_2 = \omega \frac{M^2}{L_p} I_2^2 Q_2 \tag{2.9}$$

where Q_2 is the quality factor of the secondary side that is compensated by the receiver compensation circuit. According to equation (2.9), the output power is directly proportional to ω, M, I_1, or Q_2.

Since the IPT system is sensitive to the frequency, increasing the frequency could increase the power but change the compensation circuit parameters. A higher frequency will cause electromagnetic interferences (EMI) which can be a safety issue in a high-power operating condition. On the other hand, increasing the mutual inductance will not require any variation of the designed IPT parameters, which is the best approach to increase the power. Since the mutual inductance is constrained by the coupler size, coupler material, configuration of the coil, etc., increasing the track current will increase the magnetomotive force (MMF) on the primary side coil, thus, improve the output power while decreasing the system efficiency. Increasing Q_2 of the secondary side current is another solution, but the VA rating on the receiver circuit is increased and the bandwidth is narrowed. These factors make the design of the IPT systems complicated. In order to design an IPT system for a locomotive, the IPT design must consider four aspects:

1) Coupler design;
2) Compensation circuit and system design;
3) Controller design;
4) Electromagnetic interference (EMI) standard investigation.

The coupler is one of the most critical parts of an IPT system. It is comprised of the transmitter core and coil as well as the receiver core and coil. The design of a coupler determines the coupling coefficient k of the system [28]. With a higher k value, more power could be transferred to the secondary side for the same track current. However, a good coupler design must also have a higher misalignment tolerance.

The k value can be improved by adding magnetic permeable materials, such as the ferrite cores, in the transmitter and receiver coil. However, the ferrite cores with high permeability can increase the cost of an IPT system significantly. Thus, there is a trade-off between the coupler cost and the coupling coefficient of the couplers. Many coupler designs are proposed in recent years to improve the power transfer capability: Korea Advanced Institute for Science and Technology (KAIST) has worked on the wireless charging for locomotives since 2010 [29 –37]. Most of their designs used an operating frequency of 20 kHz making it possible to achieve the highest power efficiency as well as a high output power with large air gaps. Figure 2.2 shows four different types of coil designs developed for railway systems. The I-type coupler displayed in Figure 2.2 (a) was developed for a 60kW IPT system with an air gap of 20 cm. The S-type coupler shown in Figure 2.2 (b) was proposed in 2015 for a 22kW IPT system. For both I-type and S-type designs, the flux directions at neighborhood poles are in opposite directions. These core designs canceled the electromagnetic field (EMF) produced by neighborhood poles and reduced the EMF for pedestrians around the power supply. However, these two designs have a null position when the pickup coils are located between two I-type or S-type core units, which cancel the magnetic field across the receiver and reduce the power transfer capability, making the designs not applicable for static charging. During dynamic charging, the system will also have a large power fluctuation that weakens the transferable power as well as affects the control system stability. Besides, the core designs consist of many core plates, which have a high core volume and lead to an expensive core material cost.

The KAIST research team also developed a 1-MW IPT system for a high-speed train with two U-type cores on the transmitter and an E-shape core on the receivers shown in Figure 2.2 (d). This design reduced the misalignment problem as well as reduced the magnetic field above the pickup with E shape core. Figure 2.2 (c) demonstrates the coupler design proposed in 2020 for railway applications. The system was validated at 12.6kW with a 23 cm air gap and achieved an 85% efficiency. Both of these designs have a much longer transmitter coil than the receiver, which is more suitable for dynamic charging. If the trains stop at a station for static charging. Most of the magnetic flux will be wasted or generate extra losses due to the small size of the receiver.

A team from Southwest Jiaotong University [38] proposed a dual transmitter and receiver coupler design for wireless locomotive charging. Figure 2.3 displays their coupler design. The system operated at 20 kHz with a 1.5 kW output power. The dual transmitter could enhance the magnetic field, and the dual receivers could capture more magnetic fields.

Finally, Figure 2.4 presents a three-phase coupler design for a railway system from Harbin Institute of Technology with an operating frequency of 20 kHz and an air gap of 30 cm. The system was operated at 5 kW with 82.7% efficiency. The coil distribution reduces the fluctuation of the output power compared with single phase I type transmitter. But the core volume is still high, which reflects on the high core material cost.
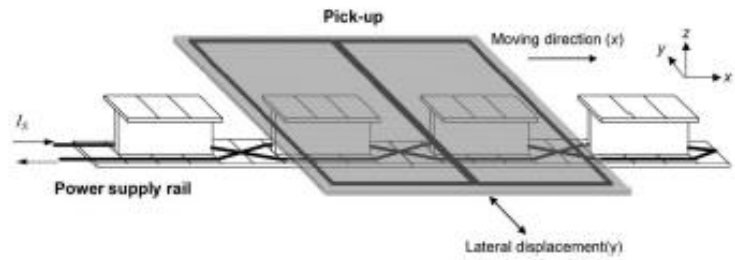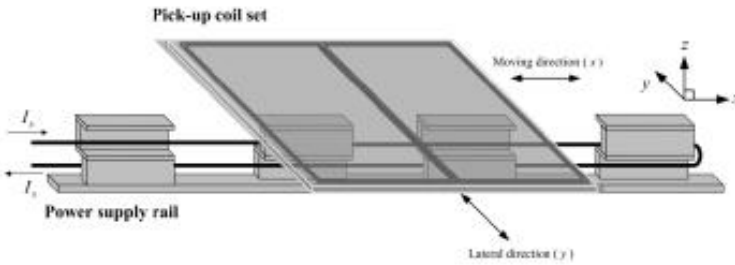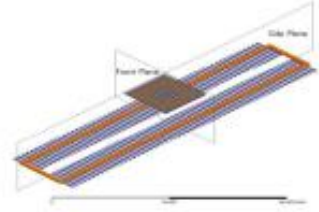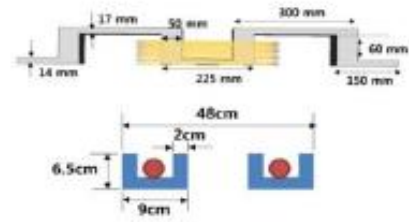
Figure 2.2 Coupler designs from KAIST team: (a) I type coupler; (b) S type coupler; (c) Rectangular coupler; (d) 1-MW project coupler. [29-31]
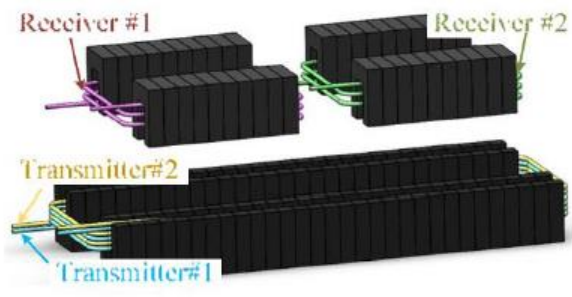
Figure 2.3 Coupler design from Southwest Jiaotong University [38]
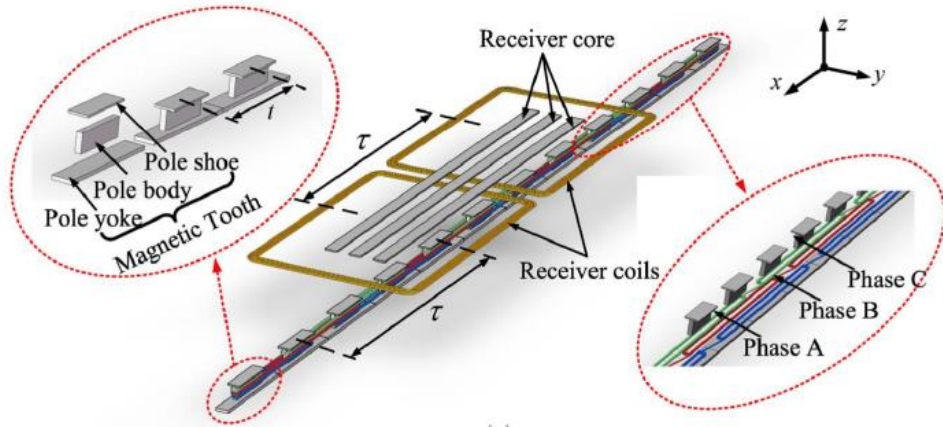
Figure 2.4 Coupler design from Harbin Institute of Technology [39]

In a loosely coupled IPT system (coupling coefficient $k < 0.5$), such as the battery charging for EVs or locomotives, the leakage inductance on the primary and secondary sides are relatively high compared to conventional transformers. Hence, the leakage inductance is compensated by provide more power to the receiver, at the same time, reduce the source VA rating. The requirements of the compensation circuits are concluded as follows [40, 41],

1) maximize the power transfer capability;
2) minimize the VA rating on the source side and load side;
3) provide a constant current or constant voltage output;
4) avoid the bifurcation phenomena [40];
5) increase the system efficiency.

Figure 2.5 shows the four basic compensated topologies, SS, SP, PS and PP, where the first S or P stands for the series or parallel compensation on the transmitter (primary) side and the second S or P represents the series or parallel compensation on the receiver (secondary) side [41]. S compensation on the primary side provides a large VA rating at the input while the P compensation on the primary side has a low VA rating at the power supply. The compensated capacitor Cp is independent of the load in S compensated primary, but Cp in P compensated primary is a function of the load. In series compensated secondary side, the load is required to be small for maximum power transfer; whereas the load should be large in parallel compensated secondary side. The series-series topology is the easiest topology to design an IPT system because the system can work at frequency independent coupling factor and load. However, the transmitter coil current may have over current issue during a low coupling coefficient condition. Therefore, the communication between the transmitter and receiver is required to control the track current.

The parallel-parallel topology is also a good choice for the design because of the low VA rating at the transmitter side as well as the pure current source characteristics on the receiver side - which is more suitable for battery charging [42]. However, the change of the coupling coefficient will affect the resonant frequency as a result of the equivalent capacitance change, which increase the complexity of the controller design. Besides the basic compensation topologies, the LCL

18

compensation [43], LCC compensation [44] also become competitive compensation topologies applicable to the IPT system.
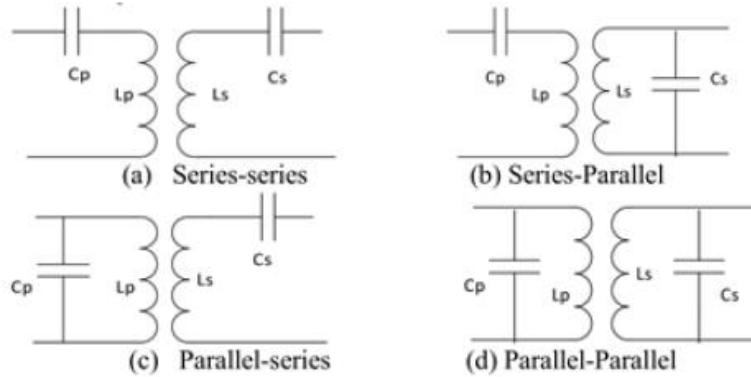
Figure 2.5 Basic compensated topologies for IPT system: SS, SP, PS, PP.

2.2. Challenging Issues Associated with Inductive Power Charging

The application of the IPT system for charging locomotives is facing several challenges. One of the key technical challenges is that the general coupler design for EVs, such as the circular pad, DD coupler [6], and DDQ coupler [45], cannot meet the design requirements for wireless train charging. An IPT system for charging locomotives needs much higher power rating and a more flexible charging space to ensure the parking spot tolerance will not severely affect the power transfer capability. A modular design is more suitable for the railway system, which can be extended easily to achieve a high-power rating and compensate for parking spot tolerance. Furthermore, coupler designs for the railway application, such as S-type coupler [36] and I-type coupler [29], have the null position issue that was discussed in previous section, which significantly reduces the power transfer capability during misalignment and leads to power fluctuations during dynamic charging.

An ideal IPT system should have high compatibility to dynamically charge the locomotives when they are entering or leaving the stations and to charge the trains when they are parked in the station. The coupler design must be compatible with both dynamic and stationary charging. Furthermore, current coupler designs mostly have high core volumes, which increases the core material cost. The ideal coupler design for the railway system should be cost-effective and maintain its power transfer capability. Hence, the IPT electrical system needs to be co-designed with the magnetic couplers to maximize the performance for high efficiency and better system stability. The system is also required to eliminate the communication between the transmitter and receiver to simplify the system and keep it robust.

2.3. Rail Track Interferences – Electromagnetic Interference (EMI)

In loosely coupled IPT systems, the leakage flux is relatively high and should be constrained to meet the requirements of the standards for human safety. There are four standards regarding EMI in the low-frequency range: The first standard is the ICNIRP 1998 / ICNIRP 2010 [46] which is published by the International Commission on Non-Ionizing Radiation Protection (ICNIRP) that provides scientific recommendation and guidance on the health and environmental effects of non-ionizing radiation (NIR) to protect people and the environment from detrimental NIR exposure. In ICNIRP 2010, the average magnetic field exposed limit is 27 uT for general public exposure, while the limit is 100 uT for occupational exposure.

The second standard is Institute of Electrical and Electronics Engineers IEEE Standard C95.1 (2005) which provides recommendations to protect against harmful effects in human beings exposed to electromagnetic fields in the frequency range from 3 kHz to 300 GHz are provided in this standard. The limit is 205 uT for general public exposure, while the limit is 615 uT for occupational exposure [47].

The third standard is IEC61980 [48] and IEC 61980 1:2015 covers general requirements for Electric Vehicle (EV) Wireless Power Transfer (WPT) systems including general background and definitions for example efficiency, electrical safety, Electromagnetic Compatibility (EMC), protection from electromagnetic field (EMF) and so on. IEC 61980 2:2019 contains the requirements for the communication between EV and WPT systems when connected to the supply network. IEC 61980 2:2019 covers specific requirements for EV magnetic field wireless power transfer (MF WPT) systems.

Finally, the fourth standard is the Federal Communications Commission (FCC) rules, that require WPT devices operating at frequencies above 9 kHz are intentional radiators and are subject to either Part 15 and/or Part 18 of the FCC rules [49].

3. Research Methodology

To fill the gaps and challenges of IPT system for the railway application, a modular W-I shaped coupler is proposed, which has a relatively higher coupling coefficient and a significantly lower core volume to reduce the core material cost and maintain the power transfer capability. The modular design can be easily adapted for both static and dynamic charging. To validate the design, finite element analysis (FEA) by ANSYS Maxwell has been conducted to optimize the W-I core design for a higher coupling coefficient. The W-I shaped coupler was also compared with the current coupler designs for the railway application in terms of coupling coefficient, core material cost, and misalignment tolerance.

To determine the effectiveness of the proposed W-I topology, a small-scale model was first developed including considerations of the packaging of the coils and the power electronics needed. The simulation and operational results are then used to create the full-scale W-I system, which is constructed to validate the design. The full-scale prototype has been tested at 5 kW with a DC-DC efficiency of 92.5%, which is the highest IPT system efficiency reported for railway applications. A live demo of the full-scale prototype power transfer has been demonstrated using a battery trailer to charge a historical trolley locomotive (Belmont Trolley).

Finally, a separate IPT system using copper sheet has been commissioned to RPS and is currently validated using a scaled model.

3.1. The Wireless Power Transfer System Development

3.1.1. Railyard Site Condition Considerations

The shape and size of the coupler are constrained by the track gauge and the chassis size of the locomotives. Since the tracks are made of iron, the edge of the coupler should not be too close to the tracks, which can lead to additional magnetic losses by generating stranded eddy current within the tracks. Although the coupler length has considerable design flexibility because the standard length of a locomotive is 20 m long, a longer coupler would increase the cost considerably as well as increase the difficulty for the installation of a single-piece coupler system. The minimum required distance from the bottom of the locomotive to the top of the tracks defines the air gap between the coupler for the locomotives, which leads to the IPT system becoming a loosely coupled system.

3.1.2. Wireless Power System Design

3.1.2.1. Small-Scale Model

To develop the W-I system, we first experiment with a small-scale model with E-shaped Ferrite core (E-core) as shown in Figure 3.1. The core is constructed from two small E-cores. The small E-core dimensions are 64 mm wide, 50.8 mm long, 10.2 mm of hegh and the side blocks are 5.1 mm wide, and the center block is 10.2 mm wide. The center and side blocks are 5.1 mm in height. The specs for the E-shaped ferrite core are shown in Figure 3.2.

Several tests were conducted to validate the system design and they are differentiated into individual (one-to-one) test and multiple transmitters-to-one long receiver test. The second group is further divided into two other sub groups; the subgroups are seven transmitters-to-one long receiver considered for dynamic charging, and three transmitters-to-one long receiver considered for static charging. Each transmitter coil comprises of two E-cores, and two coil layers. Each layer

has eight wire loops. The wire is tightly packed around the core center block. The individual transmitter E-core coil is shown in Figure 3.3.
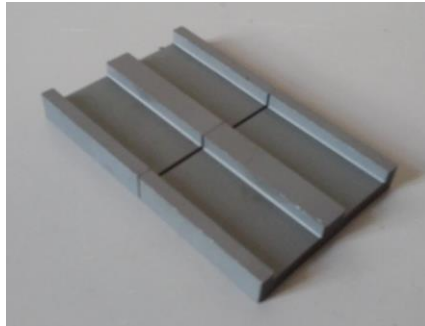
Figure 3.1 E-shaped Ferrite Core
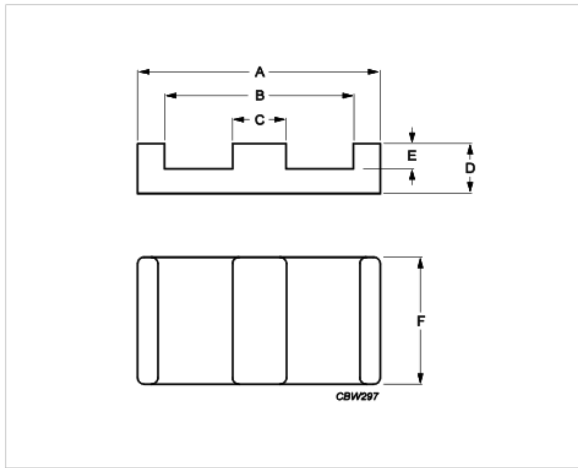
Effective parameters			
	Parameter	**Value**	**Unit**
$\Sigma(I/A)$	core factor (C1)	0.156	mm^{-1}
Ve	effective volume	40700	mm^3
Le	effective length	79.9	mm
Ae	effective area	519	mm^2
Amin	minimum area	519	mm^2
m	E64/10/50	≈ 100	g/pcs

Dimensions for product: E64/10/50						
	Nom	**Tol +**	**Tol –**	**Max**	**Min**	**Unit**
A	64.00	1.30	1.30	65.30	62.70	mm
B	53.80	1.10	1.10	54.90	52.70	mm
C	10.20	0.20	0.20	10.40	10.00	mm
D	10.20	0.13	0.13	10.33	10.07	mm
E	5.10	0.13	0.13	5.23	4.97	mm
F	50.80	1.00	1.00	51.80	49.80	mm

Figure 3.2 E-shaped Ferrite Core Specs [50]

Figure 3.3 Individual E-core Coil

For ease of fabrication, the receiver was made to have the same configuration as the transmitters. When a longer receiver is needed, such as an eight E-shaped ferrite cores case, then the same receiver or transmitter base core case are simply replicated and added together. The E-core long receiver is shown in Figure 3.4. The result is a very long coil.
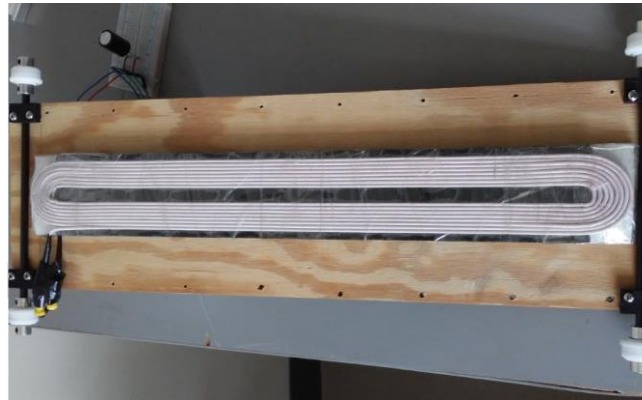
Figure 3.4 E-core Long Receiver

In this report, only the one-to-one results are presented. The one-to-one test using a single transmitter and a single receiver was first performed. Among the testes performed are vertical separation (or air gap), horizontal displacement (misalignment), and different load tests. The E-core one-to-one set is shown in Figure 3.5. The individual one-to-one ANSYS-Maxwell design is shown in Figure 3.6 and the associated electromagnetic simulation is shown in Figure 3.7.
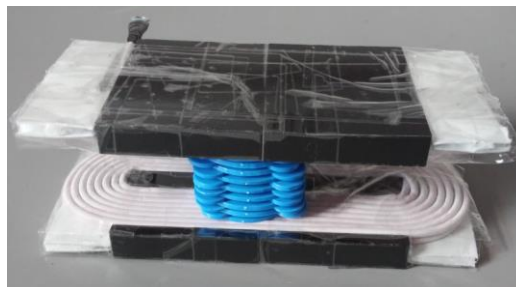
Figure 3.5 E-core One-to-One with Vertical Separation
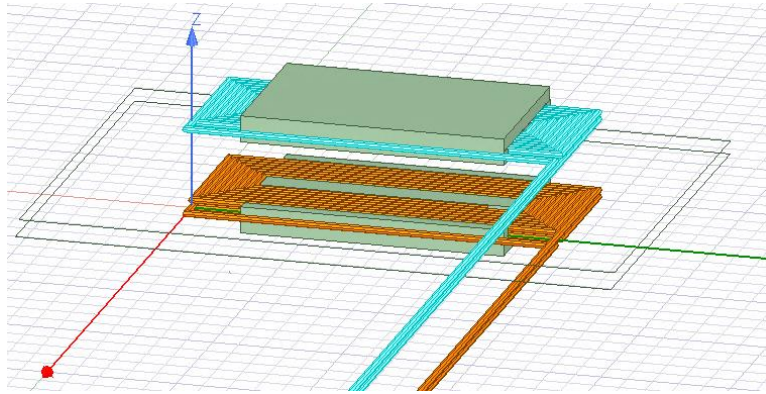
Figure 3.6 Individual One-to-One ANSYS-Maxwell Design
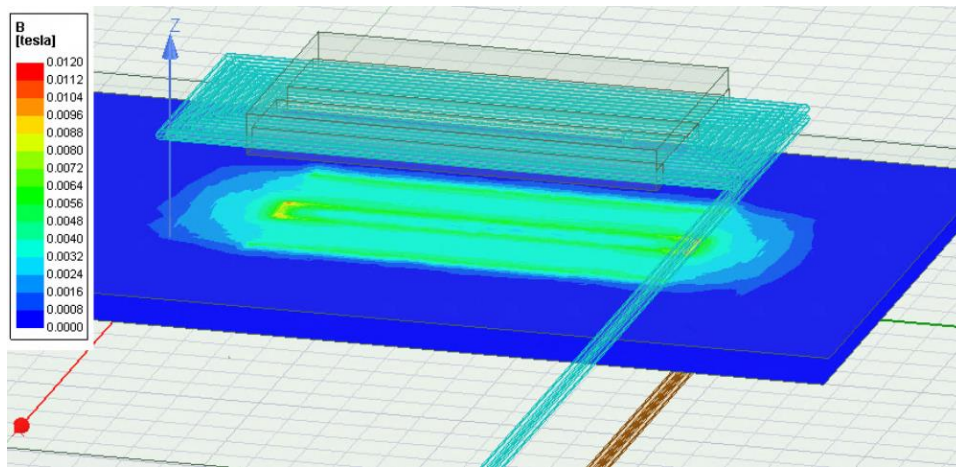
Figure 3.7 Individual to ANSYS-Maxwell Electromagnetic Simulation

The individual tests started with the vertical separation (air gap): The one-to-one ANSYS coupling coefficient simulation is shown in Figure 3.8 and the vertical separation vs voltage test result is shown in Figure 3.9. Both graphs show decreasing patterns with simulation result to be more linear than the measured results. The maximum values are 7.52 V for the measurements and 8.358 V for the simulation. The individual one-to-one vertical separation vs efficiency test is shown in Figure 3.10. The graphs are shown to have a decreasing trend. The simulation shows higher values from around 4mm to around 35 mm. The maximum values are 11.78% for the measurement and 14.56% for the simulation.

The E-core coils individual one-to-one horizontal displacement ANSYS coupling coefficient simulation is shown in Figure 3.11. The ANSYS Maxwell simulation shows a semi-linear decrease with the maximum value at 0.86.

The E-core coils individual one-to-one horizontal displacement vs voltage test is shown in Figure 3.12. The graph shows a semi linear decrease for the measurements and a semi exponential decreasing curve for the simulation with maximum values 7.5V for measurements and 8.4V for simulation, respectively.

24
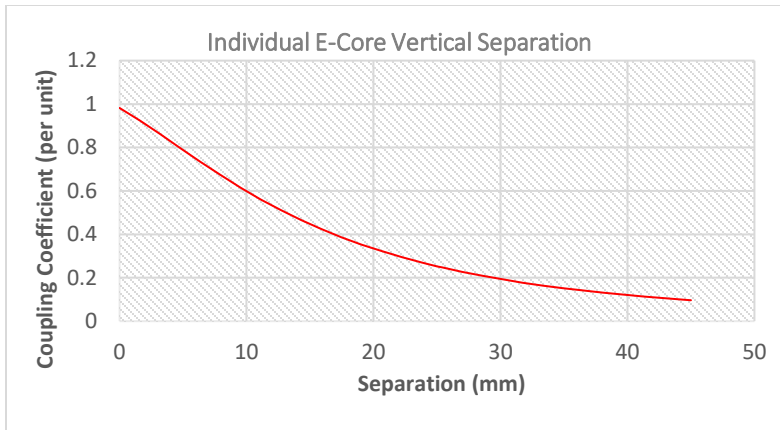
Figure 3.8 Individual One-to-One ANSYS Coupling Coefficient Simulation
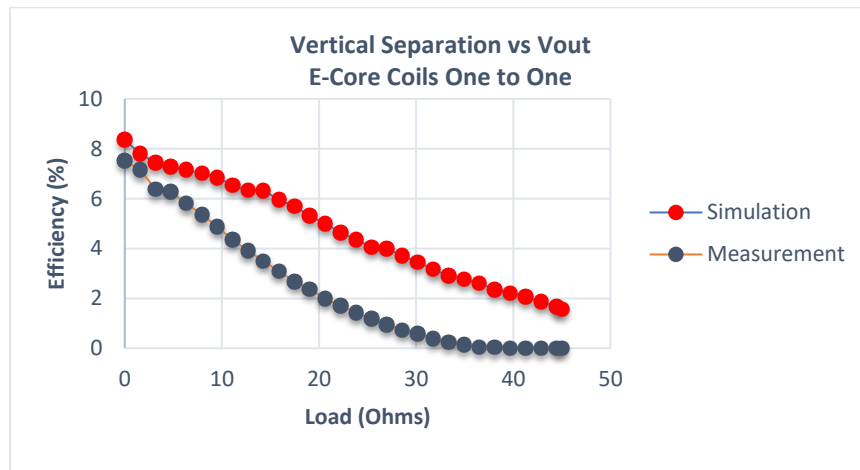
Figure 3.9 E-core Coils Individual One-to-One Vertical Separation vs V_{out} Test
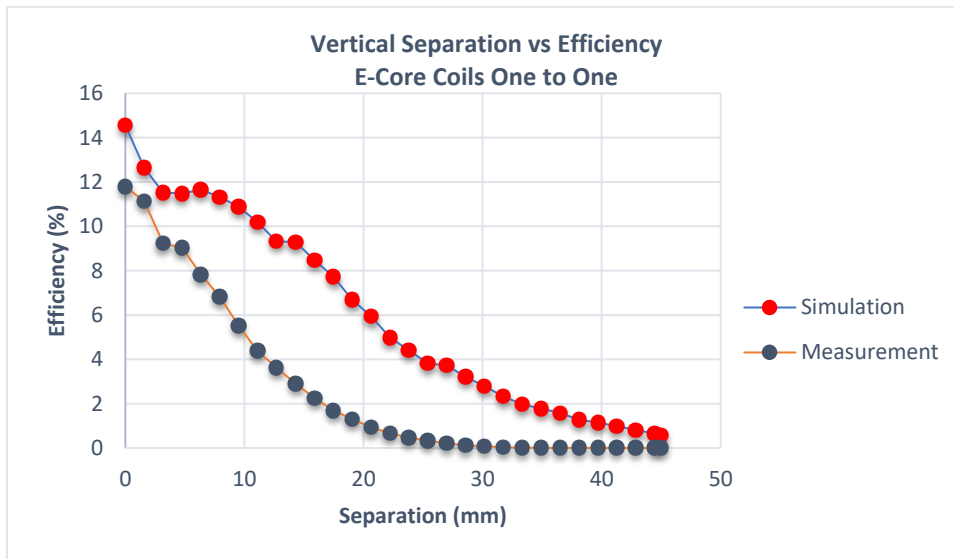
Figure 3.10 Individual One-to-One Vertical Separation vs Efficiency

25
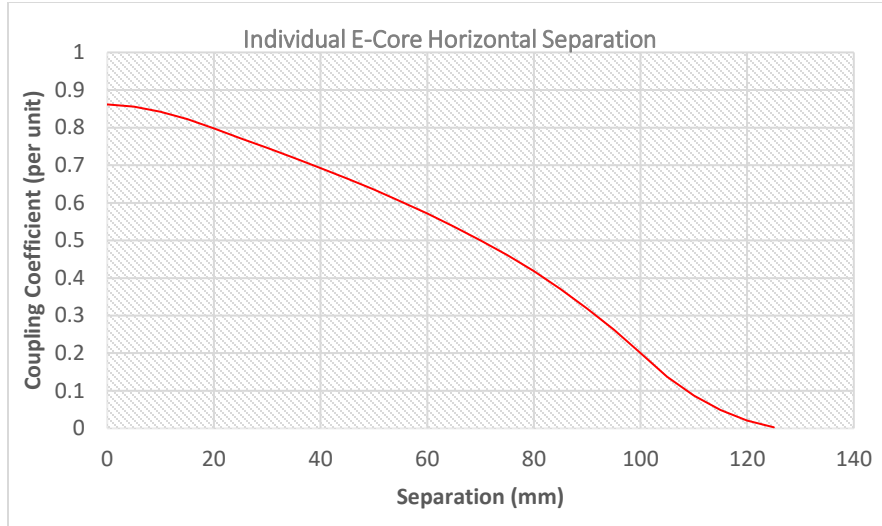
Figure 3.11 E-core Coils Individual One-to-One Horizontal Displacement ANSYS Coupling Coefficient Simulation
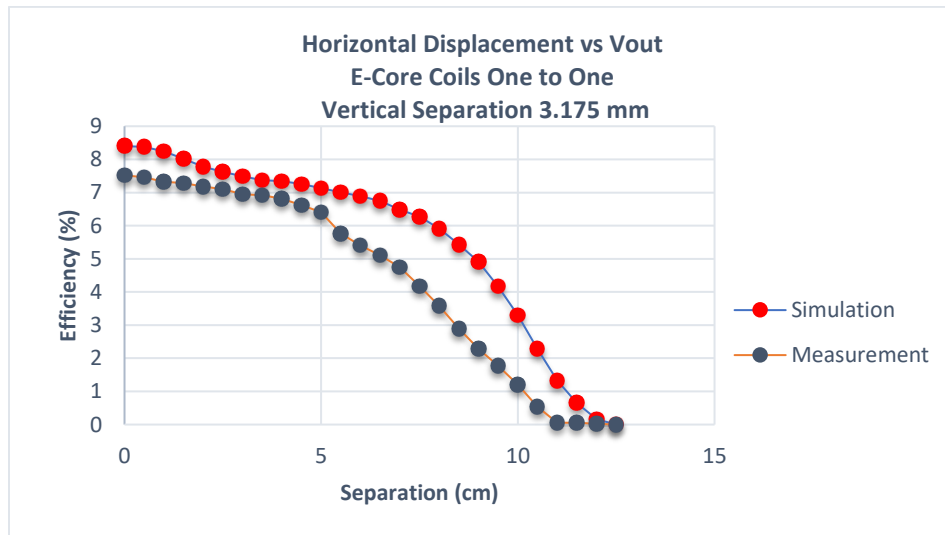
Figure 3.12 E-core coils Individual One-to-One Horizontal Displacement vs Voltage

   The E-core coils individual one-to-one horizontal displacement vs efficiency test is shown in Figure 3.13. The curves are decreasing and the simulation shows higher values than the measurements from 0 cm to 10 cm with maximum values 11.78% for the measurements and 14.70% for the simulation.

   Finally, the E-core coils individual one-to-one load vs voltage test is shown in Figure 3.14, indicating a semi exponential increase. The graphs have similar values except for the test at 5 Ohms; whereas, the simulation shows higher values at 5 Ohms. The maximum values are 7.52 V for the measurement and 8.38 V for the simulation.
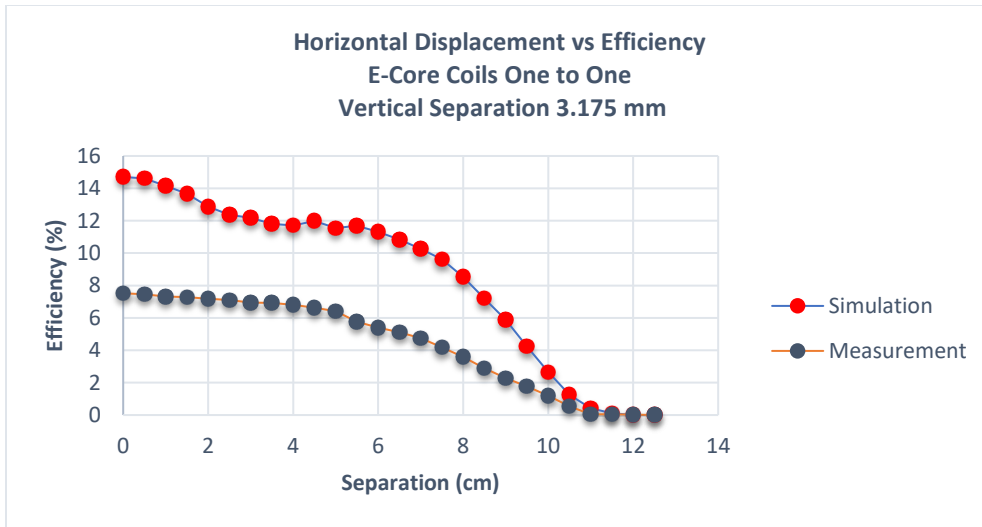
Figure 3.13 E-core Coils Individual One-to-One Horizontal Displacement vs Efficiency
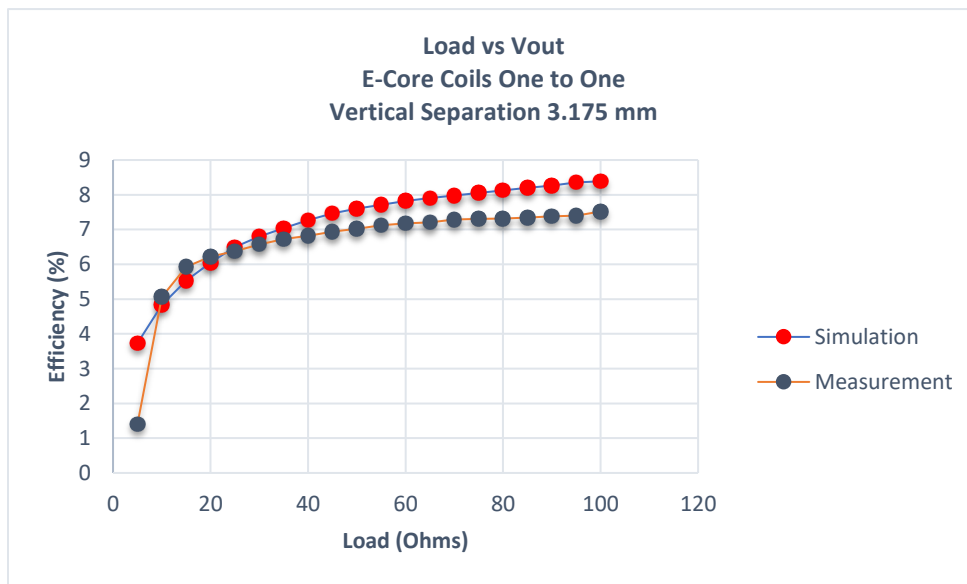
Figure 3.14 E-core Coils Individual One to One Load vs Voltage

The load vs efficiency test is shown in Figure 3.15. The graphs show a polynomial increase. The simulation shows higher values from 50 Ohms to 100 Ohms.

The final list for materials used is shown in Table 3-1. The materials are shown in Figure 3.16 and Figure 3.17.
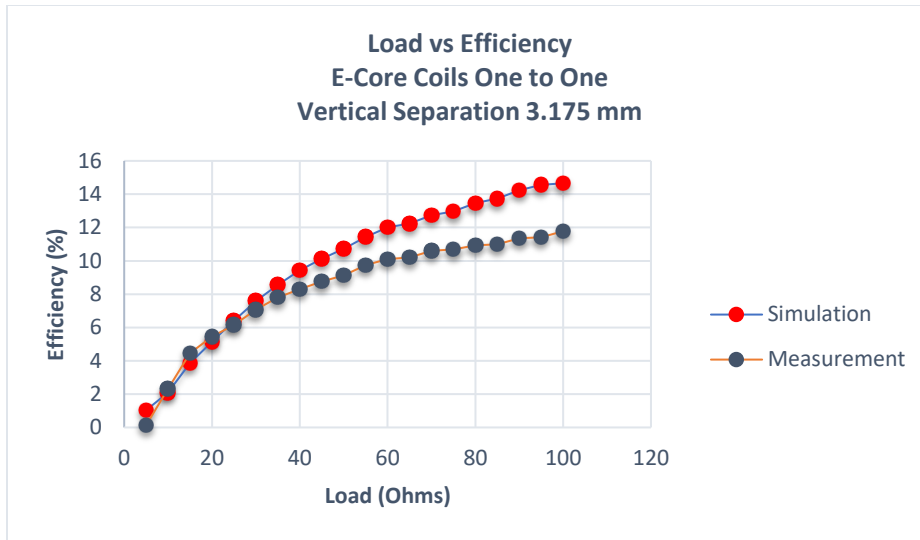
Figure 3.15 E-core Coils Individual One-to-One Load vs Efficiency

Table 3-1 Materials List

Part Name	Vendor	Quantity	Item Number
Power Supply	Digikey	2	285-1825-ND
Rectifying Capacitor	Digikey	2	493-14604-1-ND
Potentiometer	Digikey	2	CT2155-ND
ACtoDC 5V Converter	Digikey	2	945-3190-ND
USB Adaptor	Digikey	3	1568-1300-ND
Perforated Board	Digikey	2	1568-1129-ND
LCD Display Voltmeter	Digikey	4	1528-1141-ND
Power Switch	Digikey	1	360-1927-ND
Power Cord	Digikey	1	Q110-ND
Tape	Digikey	2	3M9848-ND
Terminals	Digikey	50	A1072CT-ND
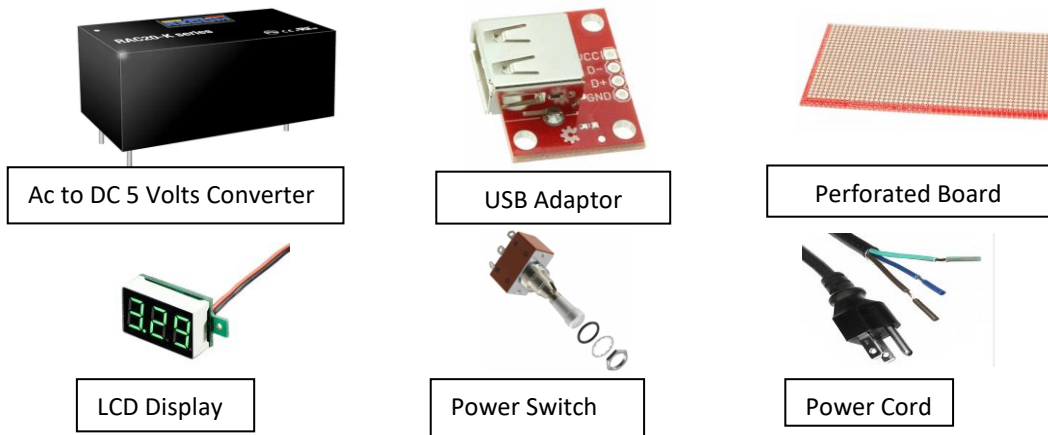
Figure 3.16 Prototype Materials
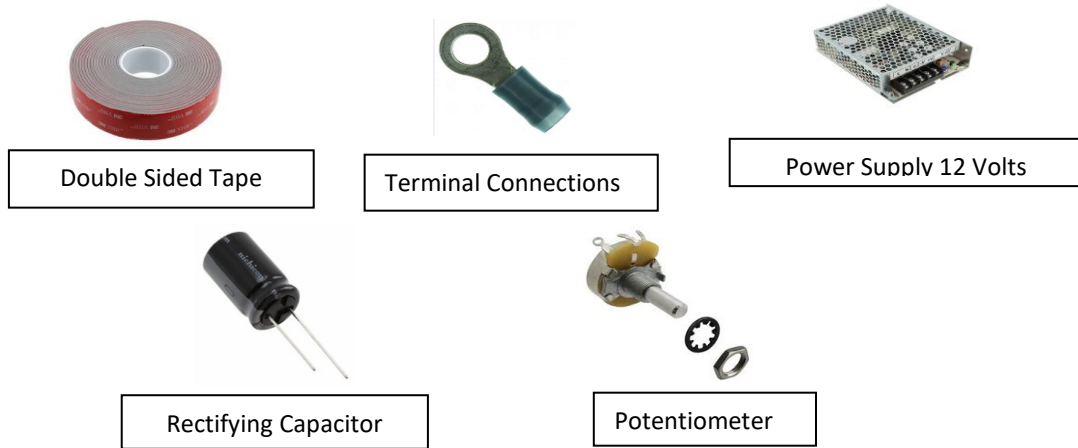
Figure 3.17 Additional Power Electronics

A 12V power supply was used to power the two half H-bridge inverters. The rectifying capacitor was used to mitigate the ripple from the output voltage. A potentiometer tested different loads and a AC-to-DC 5V converter was used to power the TI control/CARD R1.3 that controlled the inverters. The perforated board was used to host the AC to DC 5V converter and the UBS adaptors. The LCD display voltmeter was used to display the output voltage. A power switch connected the 12V power supply and the AC to DC 5V converter to the power cord. The power cord was then connected to the power outlet. The terminals were used to connect the inverter outputs to the transmitter coils, which also connected to the transmitter and receiver coils. The system connections controller block diagram is shown in Figure 3.18. Initial design used power supplies connected to the H-bridge inverters and the TI control/CARD R1.3 boards, separately. A revised modular prototype comprised the power supply and power converter inside one enclosing. The power transmission block diagram is shown in Figure 3.19.

The power transmitted worked separately from the power electronics, and it is provided by an external power supply. The power supply was connected to the H-Bridge inverter input and the inverter converted the DC signal into high frequency AC signal. The H-bridge output connected to the transmitter coils powering them with the high frequency AC. The power was transferred wirelessly to the receiver coils. The receiver coils powered the AC to DC rectifier. Finally, the rectifier connected to a load.
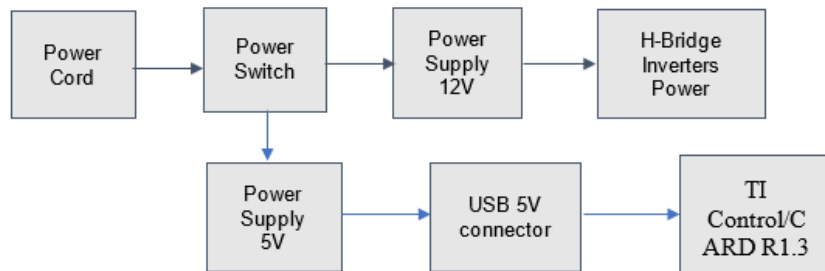
Figure 3.18 Connections Controller Block Diagram
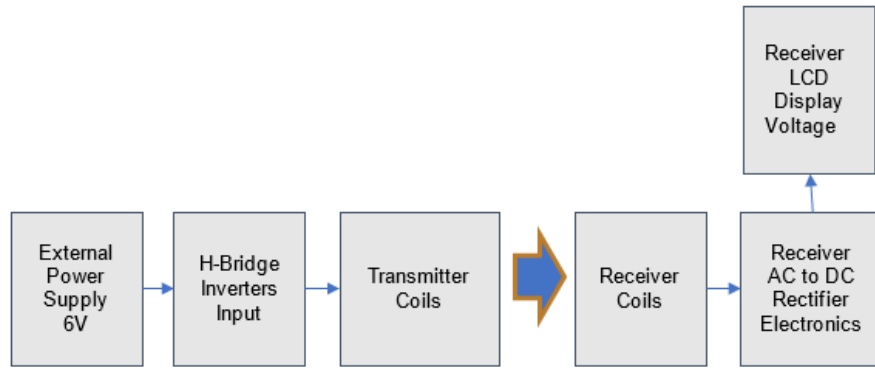
Figure 3.19 Connections Power Transmission Block Diagram

The electronics box module comprised the H-bridge inverter, the TI Control/CARD R1.3, the power electronics components to make up the prototype modular and is shown in Figure 3.20. The terminal connections are shown in Figure 3.21. The Additional components, which included the power supply 12 V, the converter assembly with the USB adaptors, and the power cord and power switch connections, are added to the electronics module and are shown in Figure 3.22. The LCD display voltmeter is positioned on the receiver side electronics housing. The receiver LCD display voltmeter is shown on Figure 3.23.

Figure 3.20 Electronics Box Module

Figure 3.21 Terminal Connections
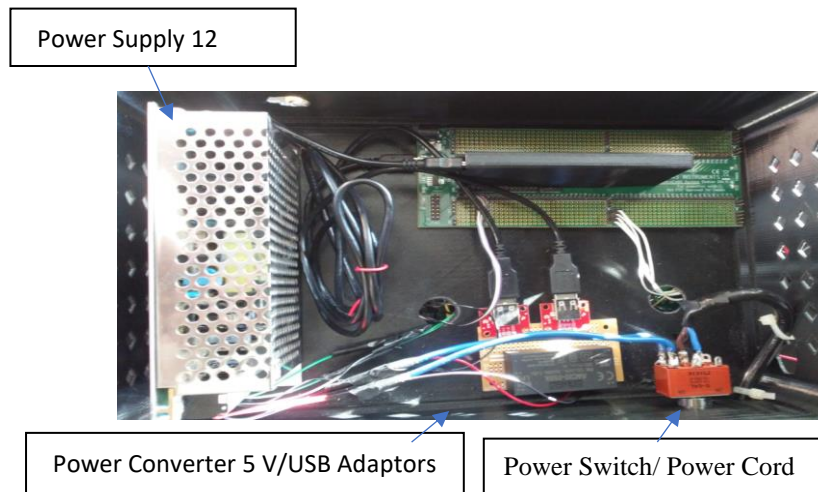
Figure 3.22 Additional Components for Modularity

Figure 3.23 LCD Display Voltmeter

To reduce the effect of ferrous materials, plastic rails were used for the transmitter base. The rails were 3D printed and were placed on a wooden base with engraved channels. The channels run longitudinal and horizontally; they are meant to house metal bars for testing different ferrous effects such as rebar in reinforced concrete slabs. The wooden base with plastic rail tracks is shown in Figure 3.24.

Figure 3.24 Wooden Base with Plastic Rails

3.1.2.2. W-I System Design

The takeaway from the small-scale IPT system is that the shape and size of the coupler are constrained by the track gauge and the chassis size of the locomotives. Since the tracks are made of iron, the edge of the coupler should not be too close to the tracks, which can lead to additional magnetic losses by generating stranded eddy current within the tracks. Although the coupler length has considerable design flexibility because the standard length of a locomotive is assumed to be 20 m long, a longer coupler would increase the cost considerably as well as increase the difficulty for the installation of a single-piece coupler system.

The minimum required distance from the bottom of the locomotive to the top of the tracks defines the air gap between the couplers, which leads to the IPT system becoming a loosely coupled system. The power transfer capability is directly affected by the k value. Thus, achieving a higher coupling coefficient k becomes one of the main objectives to improve the power transfer capability of the IPT system. Towards this goal, core material with a higher permeability is required to achieve a higher k value.

Currently the proposed couplers for train applications such as the I-type coupler designs have relatively high k values, but they also require precise positioning such that the power transfer

capability is fully realized. Since it is difficult to park the locomotive at an accurate spot, it is inevitable for a locomotive to park at a null position with almost zero power transfer.

Based on the constraints and requirements discussed above, a W-I shape coupler depicted in Figure 3.25 is proposed for the IPT system for railway application. The coupler consists of a W-shaped transmitter (Tx) core and two I-shaped receiver (Rx) cores. The core material is Ferroxcube 3C90 which has a relative permeability of 2,300. The air gap of the coupler is designed to be 5 inches (12.7 cm). The shape and size of the coupler, as well as the position of the coils, were optimized via ANSYS Maxwell to achieve the highest coupling coefficient k which can increase the output power transfer capability. The coupler was designed to be a discrete distributed system along the tracks, which reduces the cost of the cores and increases the ease of installation.

(a)

(b)
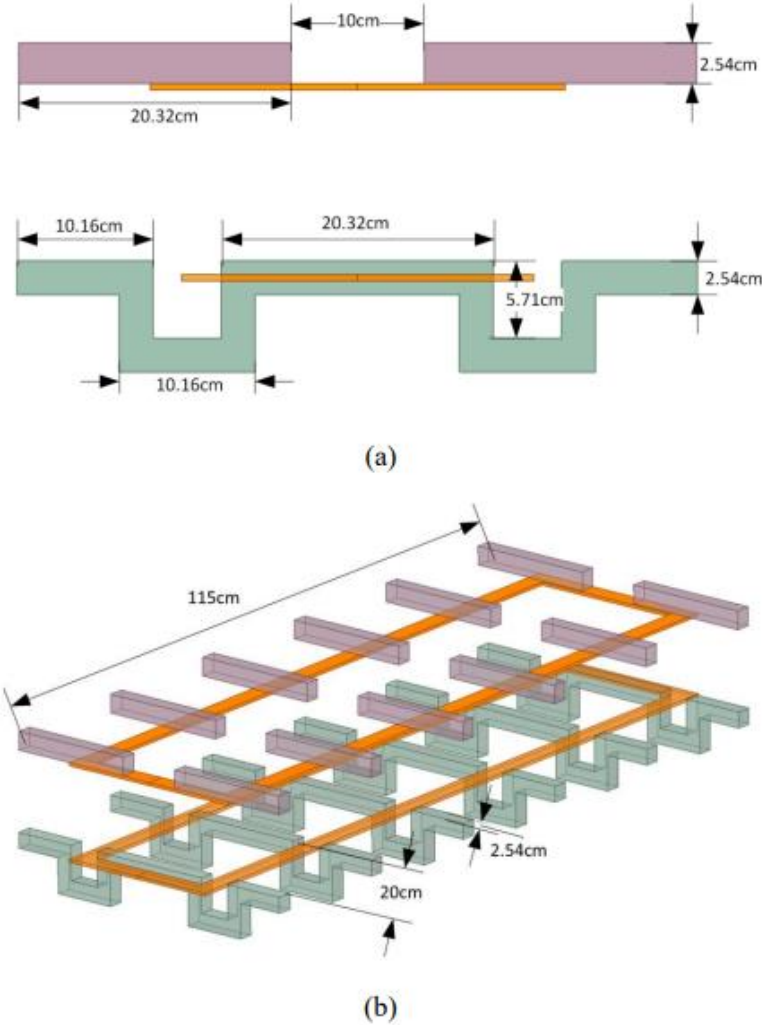
Figure 3.25 Dimension information of the proposed W-I shaped coupler (a) Overview; (b) Front view.

32

3.1.2.3. High-Voltage Hardware Considerations

In contrast to a tightly coupled systems, the loosely coupled IPT system requires the compensation circuits on both transmitter and receiver sides to reduce the VA rating on the source and load sides and maximize the power transfer capability. As stated earlier, there is some degree of difficulty in parking a locomotive at a precise charging position. Hence, a constant track current irrelative to the coupling coefficient is desired to provide a constant magnetomotive force to the receiver and ensure the stability of the power transfer process. There have been many compensation topology designs such as LCC-S and double side LCC to fulfill these requirements. The second capacitor in series with the transmitter coil increases the design flexibility. However, these designs will also increase the number of passive components to increase the conduction loss as well as affect the system efficiency. In order to simplify the compensation circuit to reduce the component and keep its benefits, an optimized LCL-S compensation topology is shown in Figure 3.26.
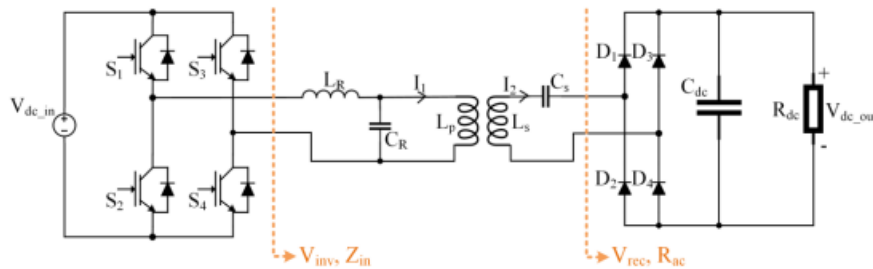
Figure 3.26 Proposed LCL-S compensated IPT system for railway application.

The codesign for electrical circuits and magnetic coupler is implemented to ensure the compensation circuit has a minimum number of passive components to maintain the design requirements and improve the system performance. The LCL-S compensation circuit also provides a constant track current which will not be affected by the misalignment and load variation. Thus, the communication between the transmitter and receiver side should be eliminated. This design will simplify the control system.

Figure 3.27 shows the equivalent circuit of the LCL-S compensation circuit. This topology removed the capacitor in series with the transmitter coil in the LCC-S topology to reduce the number of passive components in the circuit and lower the conduction loss in the compensation circuit. Due to the compensation circuits filtering the high-order harmonics, only the fundamental frequency, which is also the designed resonant frequency, is analyzed. According to the Fourier analysis, the inverter output voltage V_{inv} and the equivalent resistance R_{ac} can be derived respectively as

$$V_{inv} = \frac{2\sqrt{2}}{\pi} V_{dc\_in} \tag{3.1}$$

$$R_{ac} = \frac{8}{\pi^2} R_{dc} \tag{3.2}$$

where V_{dc_in} is the input DC voltage and R_{dc} is the load resistance. To minimize the VA rating, the compensation circuits are required to be operated at the resonant frequency [41]. Therefore, the design constraints of the LCL-S compensation circuit are

$$\begin{cases} \omega L_R = \dfrac{1}{\omega C_R} \\ L_R = L_P \\ \omega L_S = \dfrac{1}{\omega C_S} \end{cases} \tag{3.3}$$

where L_p and L_s are the self-inductances of transmitter and receiver. By analyzing the equivalent circuit in Figure 4-2 via Kirchhoff's Voltage Law (KVL), the track current I_1 and rectifier voltage V_{rec} are derived as follows,

$$I_1 = -\frac{V_{in}}{j\omega L_R} = -V_{in} \cdot j\omega C_R \tag{3.4}$$

$$V_{rec} = j\omega M I_1 \tag{3.5}$$

where L_R and C_R are the resonant inductance and resonant capacitor on the transmitter side. According to Equation (3.4), the track current only depends on the input voltage V_{inv}, switching frequency ω, and resonant parameters in the transmitter, like L_R and C_R. The track current can be kept constant while the coupling coefficient k and the load R_{ac} vary. Based on Equation (3.5), the LCL-S compensation circuit provides a load-independent output voltage. By frequency domain analysis of the inverter output voltage and current, the high-frequency inverter is capable of achieving zero voltage switching (ZVS) while the system operates at the designated resonant frequency.
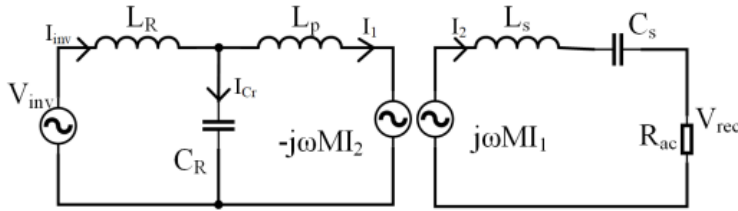
Figure 3.27 LCL-S compensation circuit equivalent circuit.

The final product is a 5 kW IPT modular system and was simulated via PLECS to validate the design. The designed parameters are shown in Table 3-2. The IPT system aims to charge an 800 V battery. Thus, a boost converter is connected to the IPT system for boosting the voltage level. Since the LCL-S topology can provide a constant track current and constant output voltage, the controller of the boost converter doesn't need communication with the IPT system. Figure 3.28 displays the circuit diagram of the IPT system design for the railway application.

The system operates at 85 kHz with an input DC voltage of 650 V. The output voltage is 800 V with an output power of 5 kW. The misalignment occurred at 1.5 s by varying the coupling coefficient from 0.22 to 0.18 which is shown in Figure 3.29. According to Figure 3.29(a), the track current keeps a constant value of 14.6 A when the misalignment occurs. The system can still provide a 5 kW output power when the misalignment occurs as shown in Figure 3.29 (b). The rectifier output voltage is decreased because of the coupling coefficient decreases in Figure 3.29(c). Thus the voltage stress on the receiver side capacitor will be increased. The rated voltage and current of the receiver side capacitor should be carefully selected to allow the misalignment

tolerance during the charging. In order to validate the performance of the W-I coupler and the LCL-S compensated IPT system design, a prototype was designed and implemented in the lab as shown in Figure 3.30. The prototype was designed to operate at 85kHz.
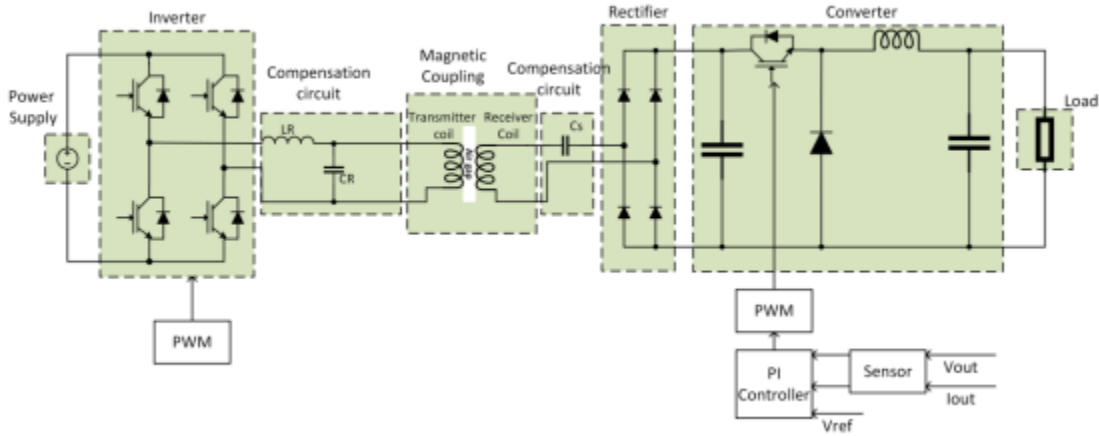
Figure 3.28 Circuit diagram of the designed IPT system

A high-frequency (HF) inverter was developed with CREE C2M0080120D Silicon-Carbide MOSFET to provide the HF power to the coupler. The components in LCL-S circuit were connected by Litz wires to alleviate skin-effect and reduce the conduction loss in the coils. Since the transmitter and receiver coils are also required to carry high voltage stress, the Litz wires are wrapped by Kapton tapes to provide the high voltage insulation. The HF rectifier is composed of four C5D50065D Schottky diodes. The material of W-I cores is 3C90 from Ferroxcube. The transmitter compensation capacitor bank is composed of eighteen B32656S2224 film capacitors to attain 48.4 nF with a 7.2 kV rated voltage. The receiver compensation capacitor bank is five HC1 high power resonant capacitors in series to obtain 20 nF with 5 kV rated voltage. The designed parameters are tabulated in Table 3-2 and the measured parameters of the IPT prototype are tabulated in Table 3-3. The measured coupling coefficient is 0.215 at a 5 inch (12.7 cm) air gap.

The IPT prototype with the proposed W-I coupler was tested by ramping up the input voltage from 150 V to the rated 650 V with 8.5 Ω load resistance. The simulation results and testing results are shown in Figure 3.31. The simulation model is built in PLECS by taking not only the conduction losses but also the switching losses of the semiconductor devices into consideration to improve the simulating precision. The DC-DC efficiency was measured by Tektronix PA3000 Power Analyzer.
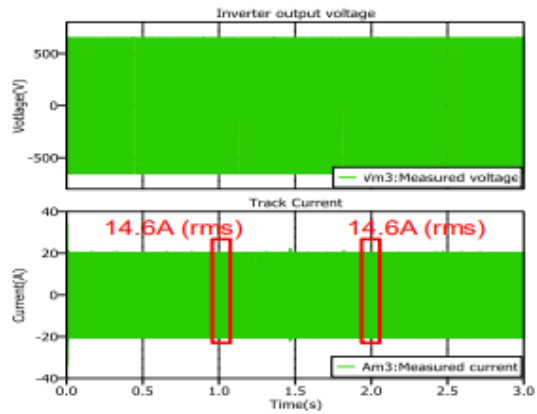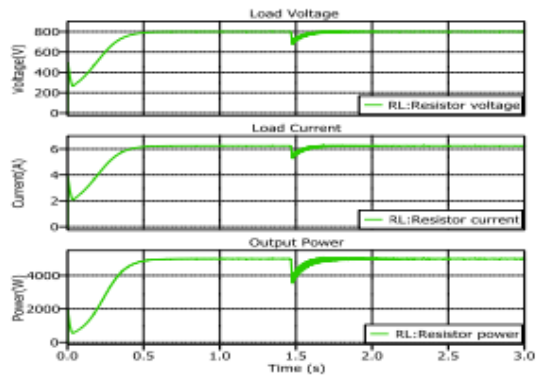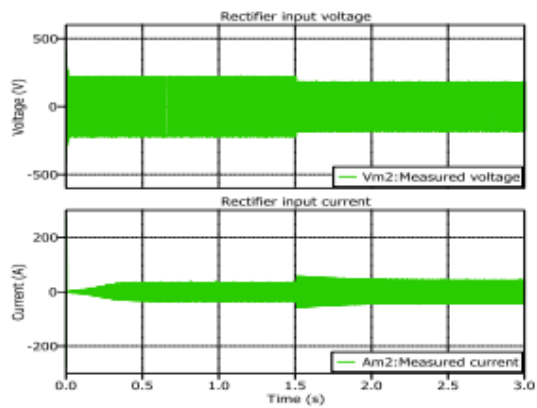
Figure 3.29 Simulation results of the designed IPT system. (a) inverter out voltage and current; (b) output information; (c) rectifier input voltage and current.

36
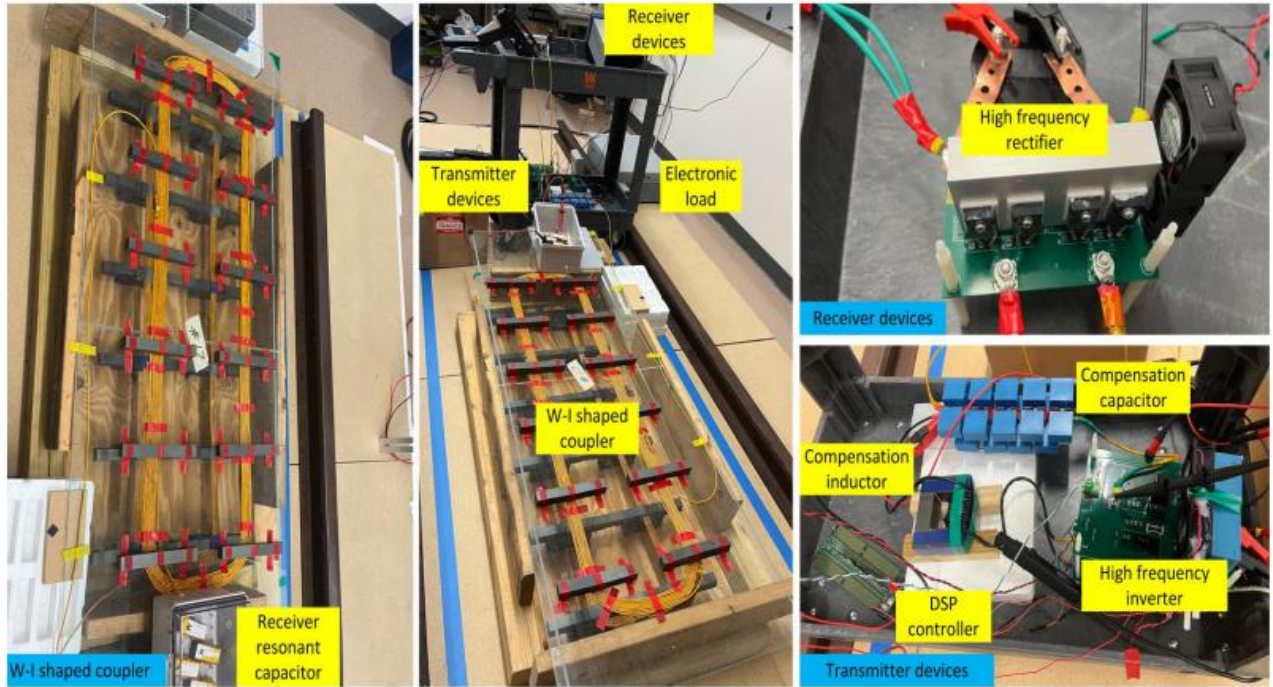
Figure 3.30 Prototype of the designed IPT system
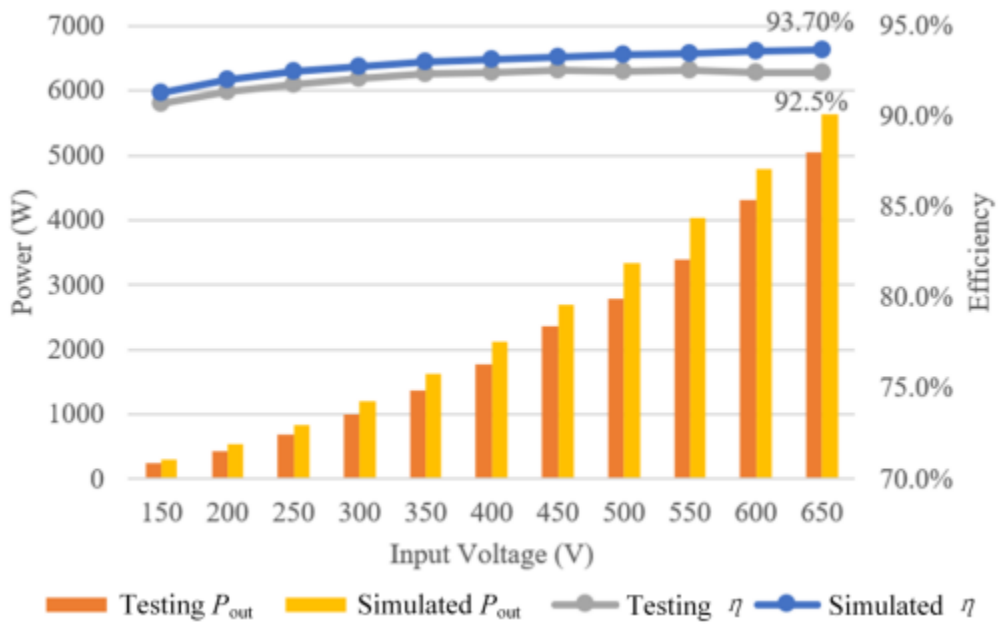
Figure 3.31 Experimental results of the output power and efficiency variation.

Table 3-2 Design Parameters

Parameter	Symbol	Value
Tx self-inductance	L_p	70 uH
Rx self-inductance	L_s	175 uH
Coupling coefficient	k	0.236
Tx resonant inductor	L_R	70 uH
Tx capacitor	C_R	50.1 nF
Rx capacitor	C_s	20.0 nF
Operating frequency	f_0	85 kHz

*Table 3-3 Measured Parameters of **the IPT Prototype***

Parameter	Measured Value
L_p	70.4 μH
L_s	174.6 μH
L_R	70.5 μH
C_R	48.4 nF
C_s	20 nF
C_{dc}	120 μF
k	0.215
f	85 kHz
R_{dc}	8.5 Ohm
Airgap	5 in

3.2. Numerical Modeling

3.2.1. Modeling Using ANSYS-Maxwell

Several modeling works in this report are performed by ANSYS-Maxwell: In solving 2D and 3D electromagnetic fields, ANSYS-Maxwell uses finite element analysis (FEA) and offers five solution types: 1) Magnetostatic, 2) eddy current, 3) transient magnetic, 4) electrostatic and 5) transient electric. Within the magnetostatic solution, ANSYS-Maxwell uses a nonlinear analysis to calculate the mutual and self-inductances, coupling factors and fields. In general, researchers have used Maxwell to validate their WPT system in terms of coil design [51, 52], coil positioning [53, 54], comparing different coil shapes [51], and validating theoretical models [55]. Misalignment has been investigated [56-58] however not to the extent of covering all three working areas of a WPT system (over-coupled, coupled and loosely-coupled). In general, when simulating most inductive WPT, most researchers have kept a minimum distance of at least the conductor's diameter between coils or double the cross-section [59].

In this study, we extended the ANSYS-Maxwell to include actual W-I system optimization and EMF and human health effect analysis.

3.2.2. Parametric Studies

Figure 3.32 shows the magnetic circuit of the proposed coupler design for optimizing the coupler geometry. The flux received by the receiver Φ_{Rx} and the leakage flux from the transmitter Φ_{Lkg} are represented as follows,

$$\Phi_{Rx} = \frac{2 \cdot mmf}{R_{gap}+R_{Rx}+R_{air}+R_{Tx}} \tag{3.6}$$

$$\Phi_{Lkg} = \frac{2 \cdot mmf}{R_{Lkg}+R_{Tx}} \tag{3.7}$$

where *mmf* is the magnetomotive force generated in the transmitter coils, and R_{Tx}, R_{Rx}, R_{gap}, R_{air}, and R_{Lkg} are the magnetic reluctance of the transmitter cores, receiver cores, airgap, and air. The coupling coefficient *k* reflects the ratio of received flux Φ_{Rx} to the total flux $\Phi_{Rx}+\Phi_{Lkg}$ [60]. Based on Equation (3.6) and (3.7), the *k* value can be expressed as follow,

$$k = \frac{\Phi_{Rx}}{\Phi_{Rx}+\Phi_{Lkg}} = \frac{1}{1+\frac{R_{gap}+R_{Rx}+R_{air}+R_{Tx}}{R_{Lkg}+R_{Tx}}} \tag{3.8}$$

The geometry of the coupler is one of the critical factors for improving the coupling coefficient k. By implementing the W shape on the transmitter side, R_{Lkg} near the transmitter increases by introducing more air reluctance in the magnetic loop compared with the regular flat plate core with the same length and thickness.
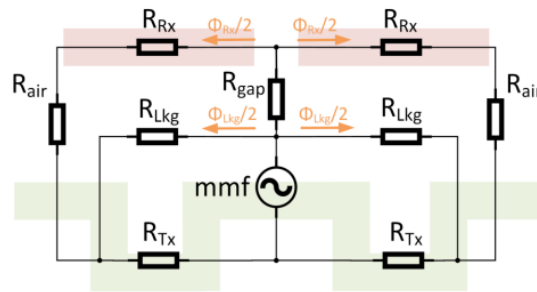
Figure 3.32 Magnetic equivalent circuit of the proposed W-I coupler.

Figure 3.33 displays the FEA results that compared the performance between a W slots core shown in Figure 3.2 (a) and a flat plate core with the same length, width, and thickness. The figure demonstrates the k value improving percentage of the W shape transmitter in different air gap distances. When the air gap is smaller, R_{gap} and R_{air} are sharply decreased to make Φ_{Rx} increase significantly. Φ_{Lkg} is reduced and takes a much smaller portion of the total magnetic flux generated from the transmitter. So the coupling coefficient between the transmitter and receiver is lifted by reducing the air gap distance. In this situation, though the W shape core reduces the Φ_{Lkg}, the impact on k improvement is negligible due to the analysis above. By increasing the air gap distance, Φ_{Lkg} takes a higher portion in the total generated magnetic flux.
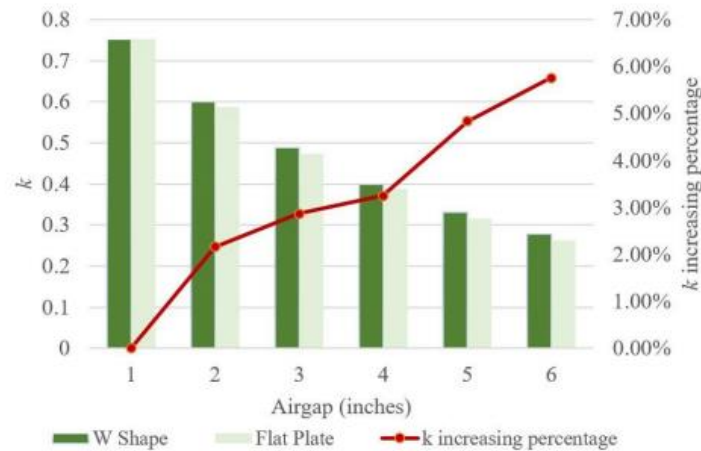
Figure 3.33 Increasing percentage of k value by varying airgap distances.

3.2.3. Electromagnetic Field Analysis

The electric industry has been concerned about safety to human body due to the influence of the electromagnetic field (EMF) generated by the WPT system including the consideration of EMF effect on medical implants such as pacemakers in the human body [61, 62]. To simulate the EMF effect on human body, an adult human body was modeled using ANSYS Maxwell and was exposed to a leaked magnetic field from a WPT system next to the rail vehicle. Two different postures were modeled: One with the person standing and one with person laying down by the railroad track. The human body model and a full-size rail vehicle with WPT system were constructed and the results show that the magnetic field exposure reference level defined by ICNIRP 2010 [63] can be generally satisfied in the human body model for both standing position and the lying down posture next to the rail vehicle.

The measurement points for EV application have been determined in J2954 [64] which suggested at 0.8 m away from the center of the WPT system. This measurement point is at the edge of the train carriage. For the railway application, however, there is no specific standard or rules for the WPT system. Hence, IEC 62957 about magnetic field levels respect to human exposure is adopted in current study [65]. This standard determines the measurement points for both inside and outside of the locomotives. The measurement point outside the locomotive is 0.3m to the surface, with different measuring heights of 0.5 m, 1.5 m, and 2.5 m. For safety purposes, the 0.8 m measurement point was selected to measure the EMF.

To help visualize and analyze the EMF in the air around the WPT system, the simulation calculation is first performed with an operating frequency of 85 kHz and with a transferred power of 5 kW. At the center point of the WPT system, a YZ place perpendicular to the coil is made, and the EMF distribution on the YZ plane is calculated in ANSYS Maxwell. The magnetic field density (without human body around the WPT system is shown in Figure 3.34. According to the ICNIRP 2010 standard [63], the magnetic field intensity of the WPT system at 85 kHz should be less than the reference level (27 µT). The adult human body model of different postures is shown in Figure 3.35. In the simulation process, the human body material properties are homogenous with average MI exposures which are frequency-dependent from 10 Hz to 10 GHz.

40
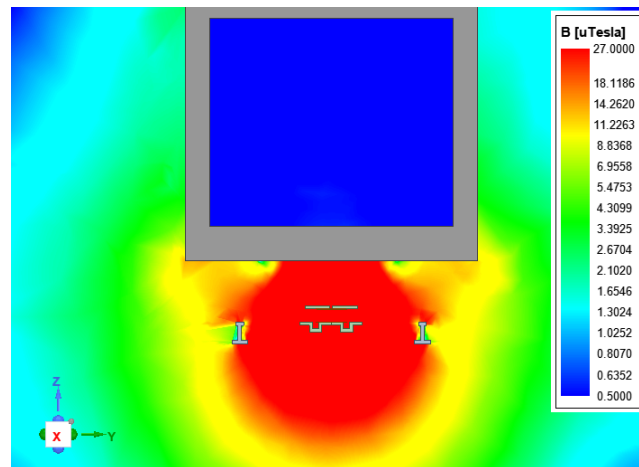
Figure 3.34 The distribution of the magnetic field intensity on cross view
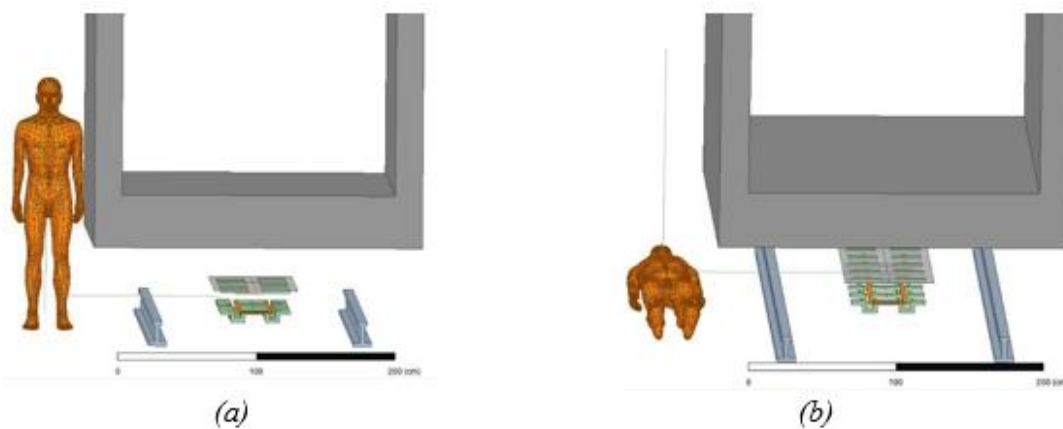
Figure 3.35 The finite element model of a human body model, a rail vehicle, and the WPT system (a) Standing; (b) lying

Figure 3.36 shows the magnetic field density distribution in the human body model, where the maximum induced magnetic field density in the human model in a standing posture was 16 µT (in the foot of the person). For the lying posture, the maximum induced magnetic field density in the human body model was 14.8 µT. The EMFs for both postures were under the reference level of 27 µT for the general public exposure as specified by ICNIRP 2010 but were larger than the reference level of 6.25 µT as specified by ICNIRP 1998. The regions where the reference level is not satisfied included the left side of the knee, foot, and head, which are shown in red in Figure 3.36 (a) and (b). And it is found that these regions are close to the coils of the WPT system. The human body model constructed in ANSYS Maxwell has geometrical accuracy in millimeter. Figure 3.37 shows the distribution of the induced magnetic field in the human model with implementing the aluminum shielding method, the maximum induced magnetic field density with both postures were at 5.9 µT, and 6.1 µT, respectively. These values meet the electromagnetic safety requirements

defined by ICNIRP 2010 and 1998. Hence, it is concluded that the magnetic field density in some small body parts can exceed the reference level defined by ICNIRP 1998 [62]. The simulation also showed that if shielding is provided, the magnetic field density can be controlled to be under the reference levels proposed by both ICNIRP 2010 and 1998.
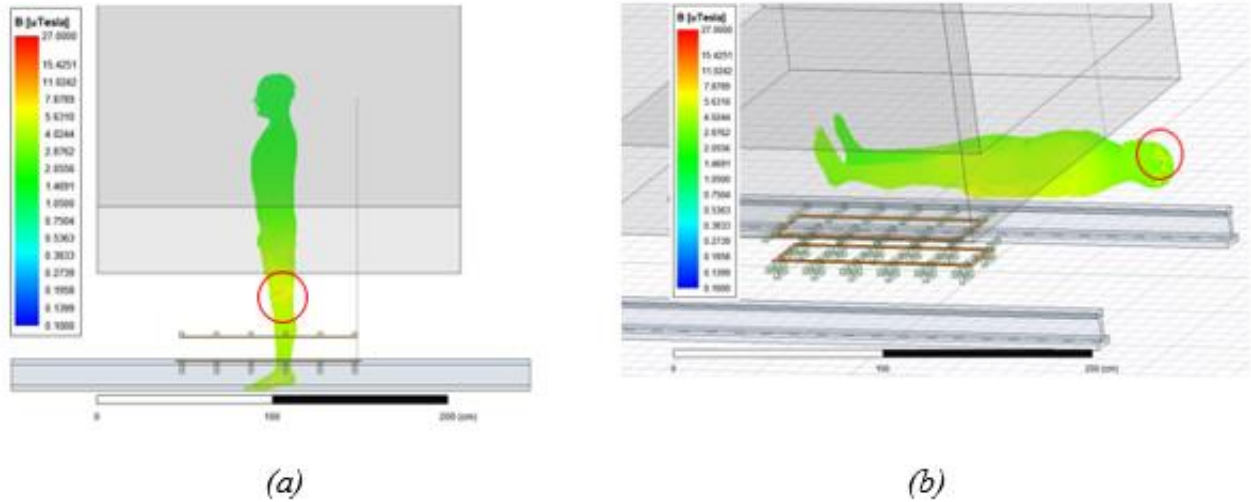
Figure 3.36 The distribution of the induced magnetic field density in the human body model (a) Standing; (b) lying
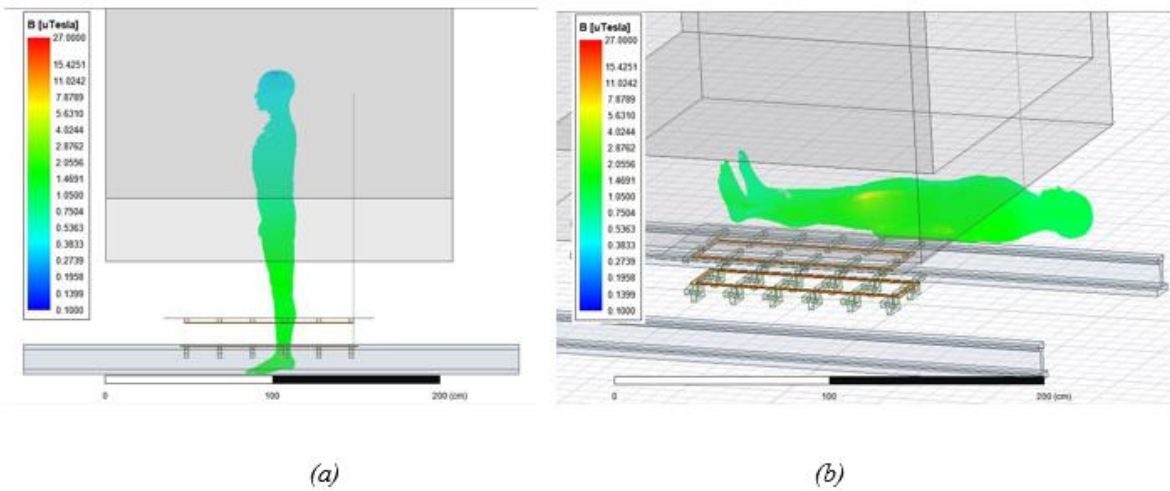
Figure 3.37 The distribution of the induced magnetic field density in the human body model (with Aluminum plate) (a) standing; (b) lying

3.2.4. Coupling Optimization

The effect of shape optimization is more obvious in improving the k value. Therefore, the W shape transmitter can improve the power transfer capability by increasing the k value in a loosely

coupled system. The coupling coefficient is enhanced by 4.8% while the designed air gap is 5 inches, which can improve the power transfer capability of an IPT system by 10%.

On the receiver side, the shape of the receiver affects the R_{Rx} value. The I-type receiver design in Figure 3.25(a) provides the shortest magnetic path compared with other shape designs, thereby having a lowest R_{Rx}. The k value is enhanced by implementing the I-type receiver. Consequently, the coupler is optimized to the W-I shape to achieve a higher coupling coefficient in a loosely coupled IPT system. Then, the dimensional optimization was conducted on the design parameters shown in Figure 3.38, which include:

- length of transmitter flanges D_{Tx_sw};
- depth of transmitter U-shape slots D_{Tx_d};
- distance between the two I-shape receiver cores D_{Rx_d};
- width of receiver coil D_{Rxc_w};
- position of transmitter coil D_{Tx_cd}.
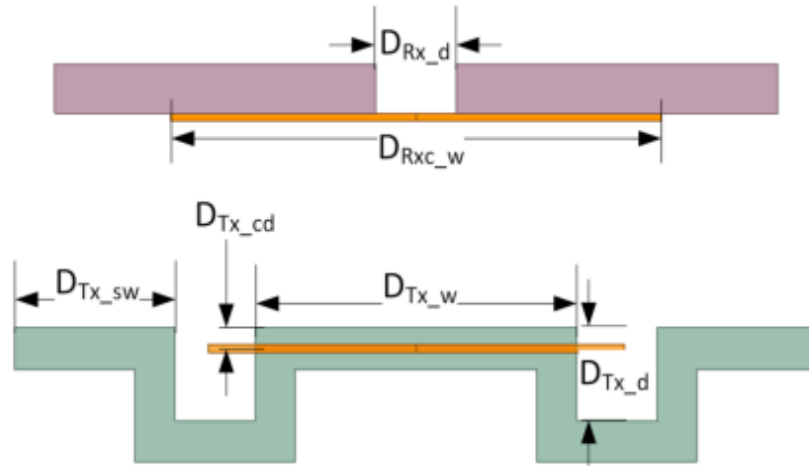
Figure 3.38 Design parameters of proposed W-I coupler

Since k is determined by the radius of both T_x and R_x coils, the width of T_x coil, D_{Tx_w}, is determined to be 20.32 cm. With varied parameters, the FEA results for k are displayed in Figure 3.39. Figure 3.39 (a) and Figure 3.39 (b) show the results for different lengths of transmitter flanges and depths of the transmitter U-shape slots, respectively. As shown, the longer D_{Tx_sw} and D_{Tx_d} are, the higher the coupling coefficient k would become. However, the increasing D_{Tx_sw} and D_{Tx_d} will become less effective to k increase and may result in more eddy current losses in the tracks. Figure 3.39(c) and Figure 3.39(d) demonstrate the k value variation by modulating the distance between two I-shape receiver cores D_{Rx_d} and the width of receiver coil D_{Rxc_w}.

The k achieves the maximum value with $D_{Rx\_d} = 10$ cm and $D_{Rxc\_w} = 25$ cm. The relationship between the position of the transmitter coil and the k value is depicted in Figure 3.39I. By lifting D_{Tx_cd} from the bottom to the top of the U-shape slots, the k value improved from 0.180 to 0.247, which increases the k value by 37.2%. Thus, the ideal position of the transmitter coil is on the top edge of the U-shape slots. However, installing and fixing of T_x coil will become difficult for

hardware development. Therefore, the final design of the W-I coupler includes the thickness of T_x coil support into consideration, which determined the D_{Tx_cd} to be 1 cm.

The relative permeability μ_r is also an important parameter, which affects the power coupling coefficient and power transfer capability. Higher μ_r will increase the coupling coefficient of the coupler, and resulted in a costly design. The FEA was implemented to vary the μ_r from 1 (same as air) to 2500 and Figure 3.40 displays the coupling coefficient as well as the output power changes while the relative permeability is increased.

According to Figure 3.40, higher coupling coefficient will improve the output power level of the IPT system. The coupling coefficient increases rapidly while the relative permeability is less than 2000, which prompts a significant increase of the output power. The increasing rate of k is less than 5% while the relative permeability is more than 2000. Thus, the relative permeability around 2000 is a reasonable selection for the core material. The core material is finally determined to be Ferroxcube 3C90 with a relative permeability of 2300.

The FEA results of the optimized W-I coupler are demonstrated in Figure 3.41 and Table 3-4. The simulated airgap is 5 inches. and the couple coefficient k is 0.236 based on the FEA results.

Table 3-4 FEA Results

Parameter	Symbol	Value
Tx self-inductance	L_p	70 uH
Rx self-inductance	L_s	175 uH
Mutual Inductance	M	26.1 uH
Coupling coefficient	k	0.236
Air gap	D_{Air}	5 in
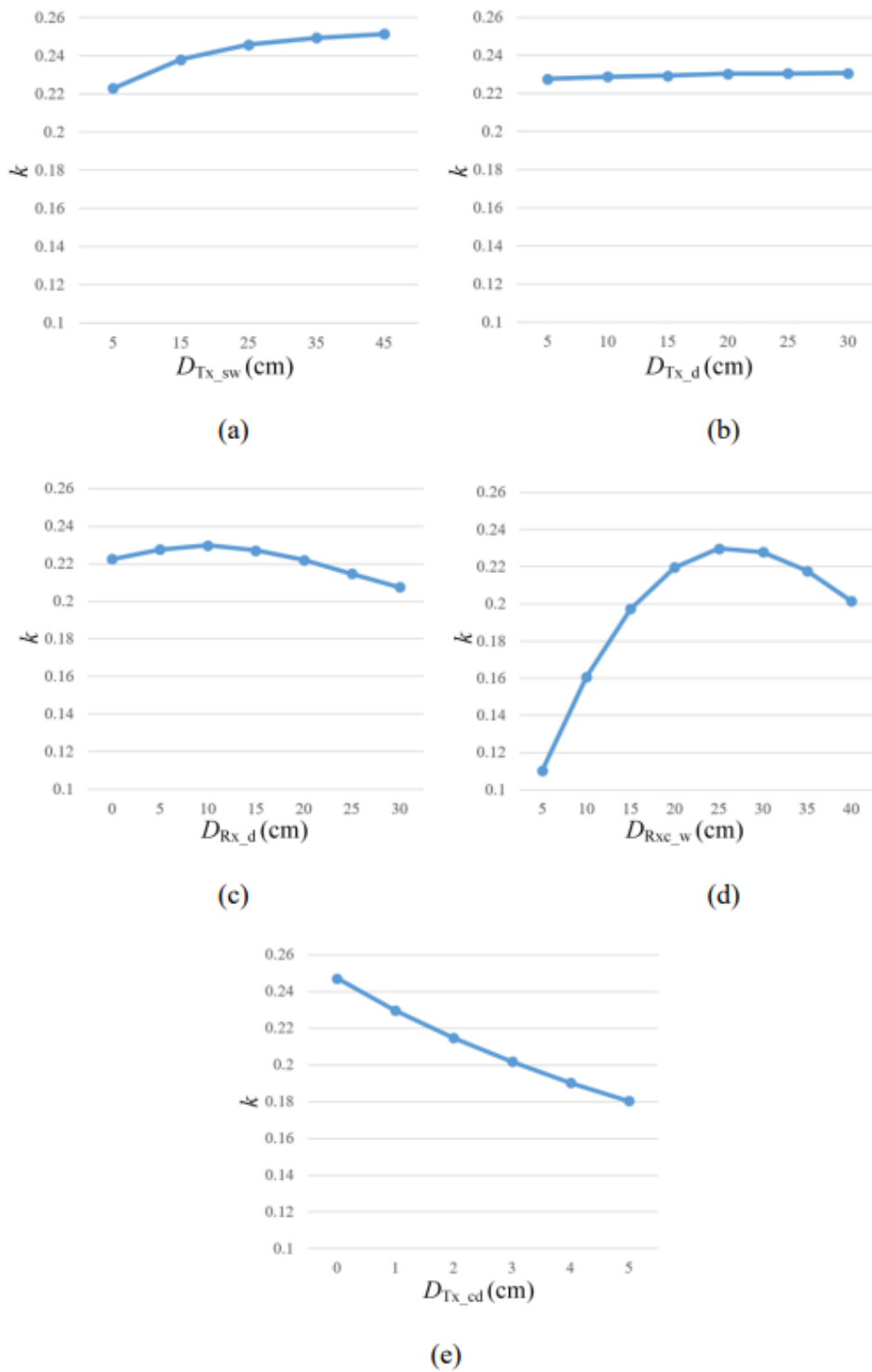
Figure 3.39 FEA results of design parameters. (a) D_{Tx_sw} vs. k; (b) D_{Tx_sw} vs k; (c) D_{Rx_d} vs k; (d) D_{Rx_d} vs k; (e) D_{Rx_d} vs k.
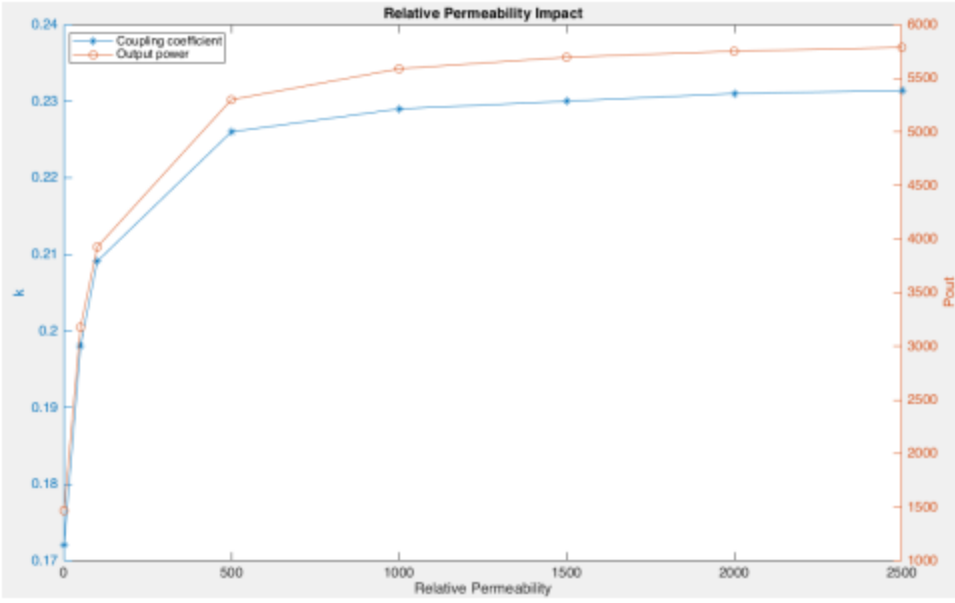
Figure 3.40 Relative permeability impact on power transfer capability

(a)

(b)
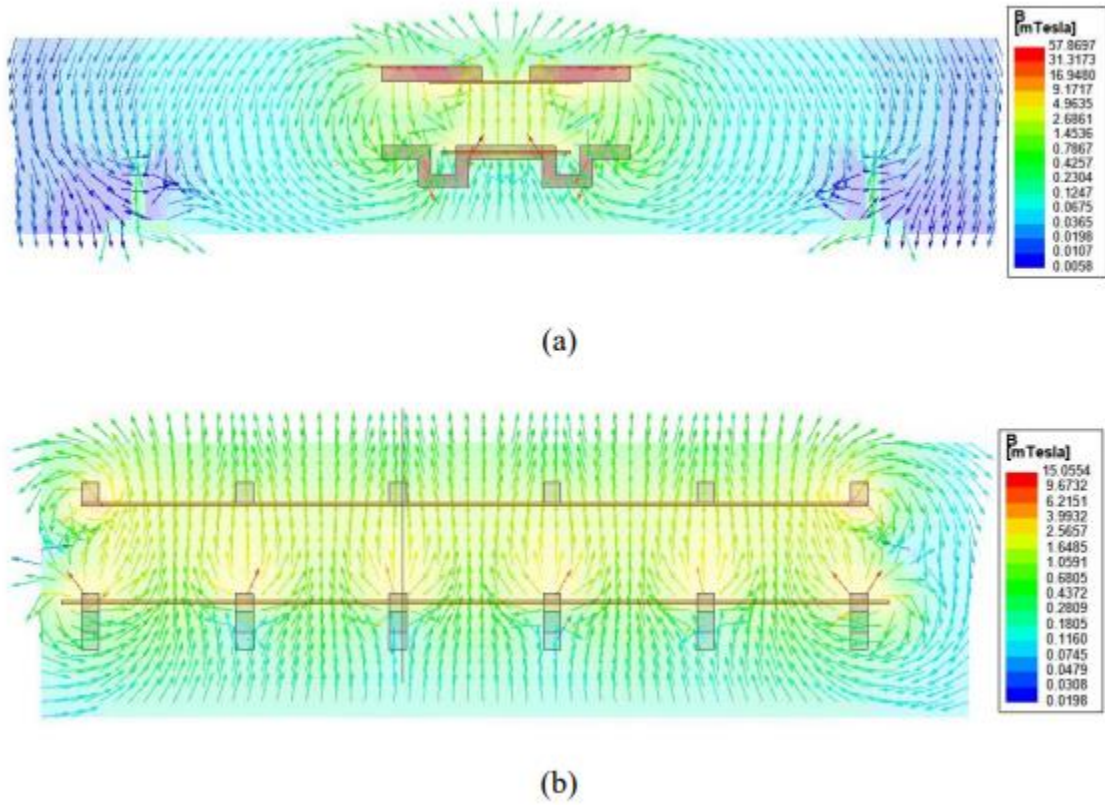
Figure 3.41 Magnetic flux density overlay of the W-I core. (a) Front view; (b) Side view.

3.2.5. Thermal Effect Analysis

Since the operating temperature of the WPT systems for rail vehicles is detrimental to the system's reliability and charging hours, thermal analysis of a 5kW wireless power transfer (WPT) system is investigated: The induction heating of the WPT system is a complex process involving both electromagnetic and thermal phenomena; therefore, ANSYS Maxwell was used to analyze the induction heating process. In ANSYS Maxwell, the calculation of the electromagnetic field is using Maxwell's equations and the calculation of the transient heat transfer in metal can be expressed by the Fourier equation:

$$Q = -\rho c \frac{\partial T}{\partial t} + k \nabla^2 T \qquad (3.9)$$

where T is temperature, Q is the heat source density induced by eddy currents, ρ is the density of metal material, c is the specific heat of the material, k is the thermal conductivity. The induction heating process combines electromagnetic simulation and thermal simulation: First, the electromagnetic simulation can calculate the ohmic loss in the WPT system. The updated result is input into the thermal simulation to calculate the temperature rise. If the temperature has not reached to steady state, then the updated temperature will be input to the electromagnetic simulation until the temperature reaches the steady state. Figure 3.42 shows the flow chart for the simulation process.

In this report, the temperature distribution is simulated using numerical analysis considering with shielding and without shielding of the receiver side. The electrical material properties and the thermal properties of the materials in the WPT system are shown in Tables 3.5 and 3.6.

The FEA result of the WPT system is shown in Figure 3.43 and Figure 3.44. The temperature distribution with shielding design is shown in Figure 3.43; it can be seen that the maximum temperature area of the ferrite bar is close to the maximum temperature of the Litz wire, which is affected by the heat conduction. High heat loss and low thermal conductivity of the ferrite bar are the reasons for the higher temperature in the central area of the ferrite bar. Figure 3.44 shows the temperature distribution for the with shielding design, and it can be seen that the aluminum plate dissipates some temperature from the ferrite bar from 45 ºC to 33 ºC. Therefore, the high thermal conductivity of an aluminum plate can be utilized between the ferrite and an aluminum plate to balance the temperature without increasing the number of ferrite bars or ferrite bar thickness.

Table 3-5 Relevant parameters of materials

WPT system Parameter	Our Design
Power rating	5kW
Primary coil turns	8
Secondary coil turns	5
Primary current, I_p	14 A_{rms}
Secondary current, I_S	26 A_{rms}
Operating frequency	85 kHz
Airgap	5 in
Room temperature	26 ℃

Table 3-6 Thermal Properties of WPT components

Component	Mass density (kg/m^3)	Thermal conductivity $(W/m°C)$
Litz Wire	8933	400
Ferrite	4600	4
Aluminum	2689	237.5
Iron track	7870	79
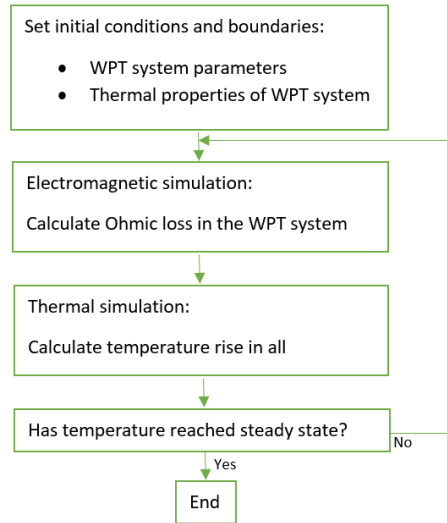
Figure 3.42 The flow chart of the simulation process
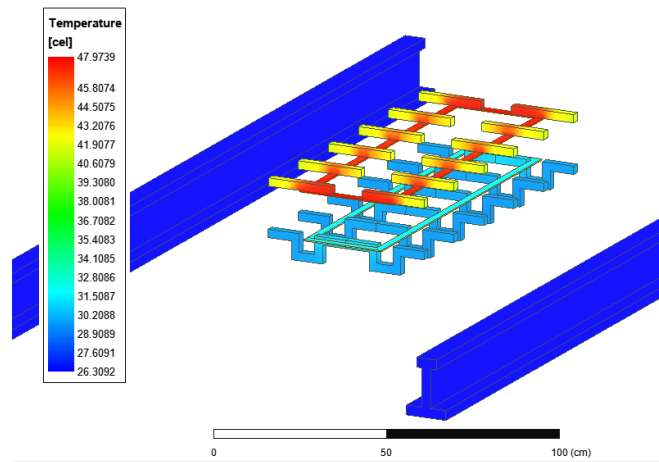
Figure 3.43 Temperature distribution of without shielding design

48
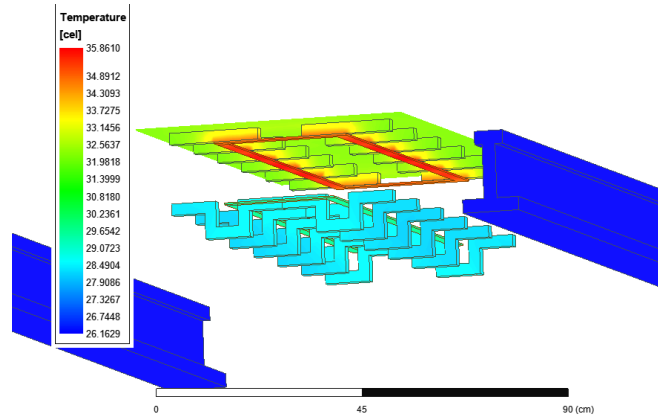
Figure 3.44 Temperature distribution of with shielding design

3.3. System Demonstration

To demonstrate the full-scale wireless power charging system, the research team joined force with Belmont Trolley and planned a one-night demonstration event at the Belmont Public Works (BPW) facility. The demonstration utilized a historical trolley, which is being modified for electrification via Lithium-ion battery technology. Figure 3.45 shows the trolley car (Figure 3.45a)) at the BPW Facility and the subsequent works to furbish a trailer car (Figure 3.45b)) equipped with a Nissan Li-ion battery pack.

(a)

(b)

(c)

(d)

Figure 3.45 The Belmont Trolley Demonstration Setup: a) The Historical Trolley Car No. 1, b) The Trailer Car, c) The Trailer Car with Onboard Li-ion Battery and Charger; and d) The Wireless Power Charging Pad between Temporary Tracks

49

The proposed system is to have a Nissan Leaf battery pack inside the trailer/light duty railcar. The addition of a battery charging port, and battery connecting cables will ensure the Li-ion battery packs will be able to be charged. The trailer/light duty railcar consist of a powertrain system to be able to move the trailer independently of the trolley as repositioning on train tracks is expected. The powertrain system will entail a chain and sprocket system, chain tensioner, and a gear motor to allow for the trailer to move independently.

3.3.1. Construction of Full-Scale Demonstration Cart

The trailer car holds one Nissan Leaf battery and assemblies including the following components: Mechanical/structural steel rectangular tube, low-carbon steel rectangular tube, steel sheet, multipurpose Neoprene foam strip with adhesive-back, Nissan onboard battery charger, Teco Westinghouse variable frequency drive, JEM-SPORT CAN to bluetooth adapter, Mouser Electronics isolated DC/DC converter 600w 400V/12V 50A, 11-12 Nissan Leaf EV 120/240V 20A charging port cable, 11-12 Nissan Leaf OEM center battery wiring harness 2976A, 3 rotary switches, 5 position, 4 pole, 10 A, 600 V, HW series, panel mount barrier terminal block, 2 row, 10 positions, 18AWG, 4AWG, 15.88 mm, 85 A, Marathon special products 985-GP-10, and the Chargepoint Homeflex NEMA 6-50 plug.

The trailer motor assembly consists of a multitude of components that are needed to transport the trailer from one trolley to another. Highlighted components include an AC Gearmotor, industrial roller chain, industrial chain sprockets, floating roller chain tensioner, adjustable slide rails, etc. The AC Gearmotor selected is a NORD 3-Phase Inline Shaft AC Gearmotor due to the torque of 350 ft.-lbs. and power of 1.35 HP required to power the trailer. The AC Gear motor selected has a power of 5 HP, with a torque of 1,250 ft.-lbs. of torque and is going to be powered by the 1 - 400 HP, 460V, 50/ 60Hz, 3-Phase, Westinghouse Inverter. The inverter is going to take the 350VDC input from the battery pack and invert the power to 460VAC. The inverter will output 3 phase power at 460VAC and the AC gearmotor can be wired for either 460 or 260VAC. Figure 3.46 shows several modifications made to the trailer car
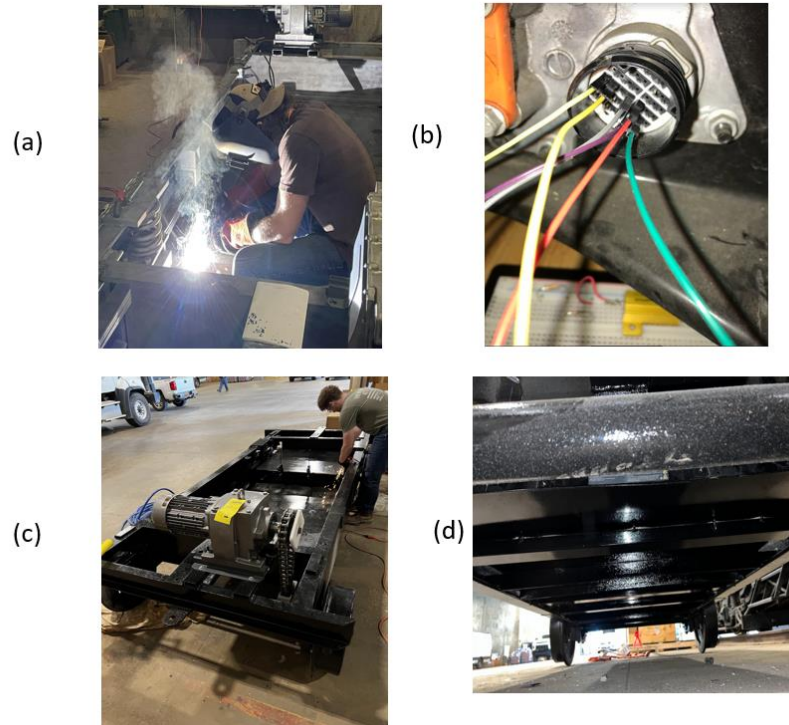
Figure 3.46 Trailer Modifications: a) Welding of battery support, b) Motor Power Connections, c) Installation of the AC Gearmotor; and d) Reinforced Trailer Chassis.

3.3.2. Demonstration at Belmont

The actual demonstration of the wireless power charging setup was performed on October 12, 2022. A night event was planned along with Belmont Trolley and the City of Belmont and was hosted at the Belmont Public Works. Since there is no railroad tracks, a 20 ft temporary track was built to allow the trailer car to travel and stop on top of the WPT pad. The event was opened to the public with several invited guests. Over 160 people have attended the event and witnessed the IPT technology and the demonstration of the charging of the battery trailer.

Because the 150 kWh Li-ion battery would take a long time to charge, a scaled display light setup was used to indicate the wireless power transfer. To remotely control the trailer car, the gearmotor was modified and coded with a Arduino Uno. Using Arduino IDE, an App has been developed for download to cell phones for controlling the motorized trailer. Figure 3.47 shows the demonstration of the trailer car moving back and forth on the tracks and power charged by the WPT pad.
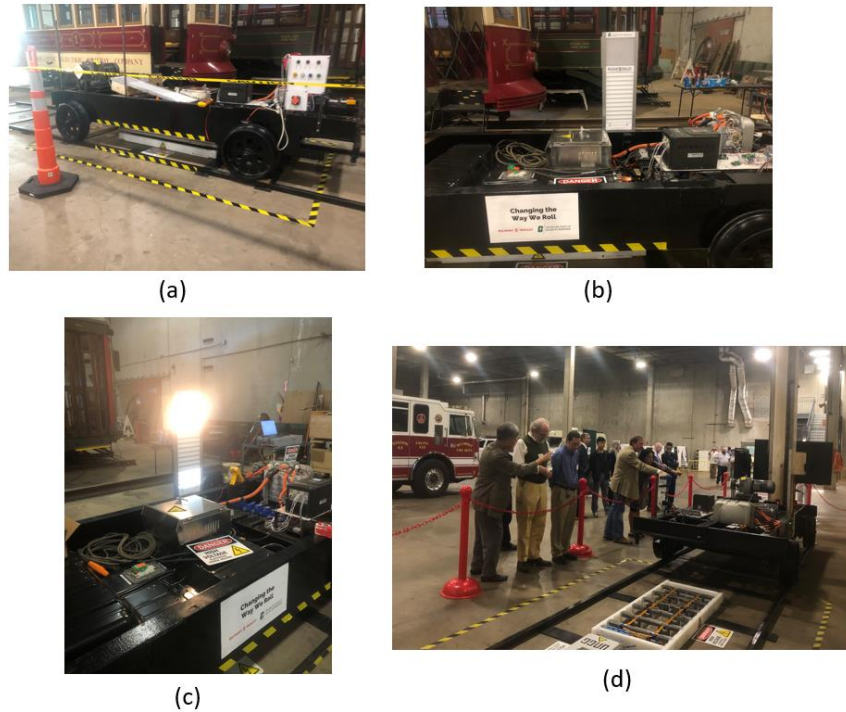
Figure 3.47 Wireless Power Charging Demonstration: a) Trailer Car Running over the WPT Pad, b) The Trailer with Light Display, c) Light Display Lit up During Charging; and d) Audience Inspecting the WPT Setup.

3.4. A Separate System Design (RPS)

A sub-scale WPT system was developed by RPS separate from the UNC Charlotte system. The goal is to demonstrate a different IPT technology using copper sheet and a single transmitter setup. The sub-scale WPT system was assembled in a mockup fashion to measure its electrical parameters for further simulation and determination of the values of external passive parts that effect its efficiency. Figure 3.48 shows the subscale system assembly. The subscale system (1/2 scale) is operating at a 4-inch air gap. System parameters were measured with East Tester ET1090 LCR meter capable of reading Inductance, Capacitance and Resistance at frequencies up to 100kHz (Table 3.7).

Table 3-7 Electromagnetic Testing Results.

Component	Inductance [uH]	ESR [mΩ]	Coupling
Transmitter	2.62	50	.445
Secondary (2 turns)	10.7	100	

*ESR stands for effective series resistance and includes both the alternating current (AC) resistance of the copper conductors that make up the coil and the AC core losses resulting from the alternating currents.

Figure 3.48 Preliminary subscale system assembly for measurement of inductance, resistance and coupling factor used in further simulations

ESR values measured were lower than the values in Table 3.7 and values of 50 mΩ and 100 mΩ were estimated for use in the simulation to consider the core loses of the ferrite plates. As an LCR meter only injects a small current of a few milli-Amperes, it cannot measure the actual core losses at AC currents as high as 290 Amp in this system. The core losses in ferrite typically increase at the power of 2.7 (as opposed to the power of 2 when squared or the power of 3 when cubed) in relation to the current oscillating in the coil conductors. The measured data above was used to simulate the system for operation at 85 kHz in Figure 3.49.

Results of the simulation indicate:

- Transmitter resonating tank current of 299 amps root mean square value (RMS)

- Transmitter resonating voltage of 404 volts RMS.

- Receiver resonating tank current of 72 amps

- Receiver resonating voltage of 501 volts

- Operating efficiency of 82%

The lower efficiency and much higher transmitter tank currents required another look at options to improve the system performance so the 2 turn coil in the receiver is planned to be replaced with a 4 turn coil resulting in a much higher inductance than was simulated in Fig 3.49. This upgrade from a 2 turn receiver to a 4 turn receiver will happen after low power testing of the mockup assembly.
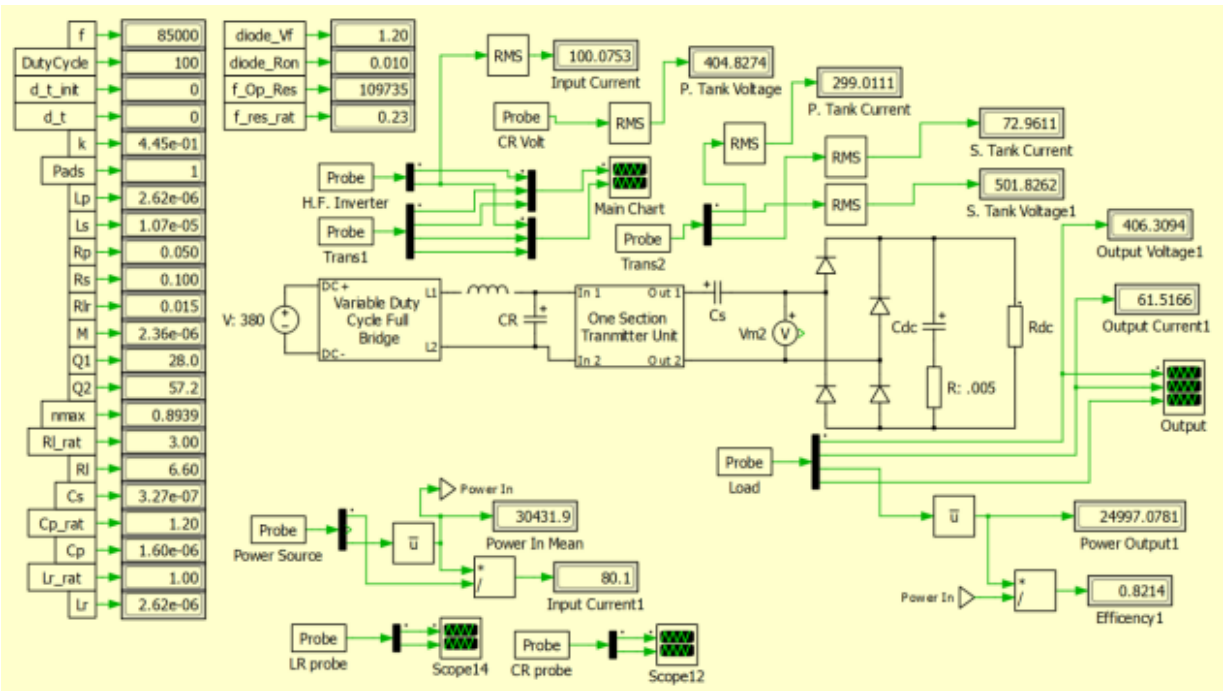
Figure 3.49 Simulation results using preliminary inductance, resistance and coupling factor

3.4.1 Low Power Mockup Testing

Figure 3.50 shows the single winding of 7.62cm x 0.056 cm copper over 4 transmitter pads (N=4) that are 81.3 cm in total length next to the receiver unit with a double winding of 5.08 cm x 0.0521 cm copper. In this case the receiver length between the cross conductors is 5 (N+1) transmitter units long. This is the configuration of hardware that was measured and simulated in Fig 1 and Fig 2 before being tested at low power in the assembly pictured in Fig 3.51.

Figure 3.50 Mockup Hardware of single turn 4 pad transmitter and 2 turn receiver

Figure 3.51 Mockup fixture of subscale system tested at low power

Initial testing of the ½ scale mockup was performed with power supplies limited to 40 volts and 30 amps. Test results presented in Fig. 3.51 shows the output power ranged from a maximum of 845 Watts down to 451 Watts. The efficiency ranged from 80 to 84%. What was adjusted between each test point was the capacitance value on the receiver side which adjusted the resonance value of the system.

90-100	100-110	Vin	Iin	Vout	Iout	Pin	Pout	E	Vp	Vs	R load	
0000	0000	36.3	29.47	76.5	11.15	1069.76	852.975	79.74%	95	580	7.25	90%
0101	0000	36.187	25.623	71.668	10.448	927.22	748.787	80.76%	81	520	7.25	94%
0110	0000	36.217	24.766	70.547	10.289	897.675	726.373	80.92%	78	520	7.25	95%
0111	0000	36.125	23.96	69.434	10.143	865.194	704.269	81.40%	75	510	7.25	96%
1000	0000	36.34	25.804	71.729	10.46	930.449	750.285	80.64%	81	530	7.25	94%
1001	0000	36.248	24.719	70.505	10.277	896.014	724.58	80.87%	78	520	7.25	95%
1010	0000	36.217	23.944	69.617	10.143	867.18	706.125	81.43%	75	510	7.25	96%
1011	0000	36.125	23.102	68.332	9.978	834.56	681.817	81.70%	74	490	7.25	97%
1100	0000	36.248	23.077	68.455	9.972	836.495	682.633	81.61%	73	490	7.25	97%
1101	0000	36.156	22.333	67.292	9.825	807.472	661.144	81.88%	71	490	7.25	98%
1110	0000	36.125	21.625	66.282	9.679	781.203	641.543	82.12%	68	480	7.25	99%
1111	0000	36.1	20.8	65.06	9.53	750.88	620.022	82.57%	66	460	7.25	100%
1111	0001	35.972	19.995	63.712	9.331	719.26	594.497	82.65%	63	450	7.25	101%
1111	0010	36.003	19.36	62.733	9.197	697.018	576.955	82.77%	62	430	7.25	102%
1111	0011	35.942	18.719	61.662	9.038	672.798	557.301	82.83%	59	430	7.25	103%
1111	1111	35.79	14.972	55.35	8.153	535.848	451.269	84.22%	47	370	7.25	110%

Figure 3.52 Test results of subscale system with two turn receiver using 40-volt power supply

In order to operate at higher power levels, the system has to be converted from an AC to DC power supply to batteries to provide the DC input power to the high frequency inverters and the DC input voltage can be raised in increments of 7.8 volts per battery module. Power supply systems are limited to 3kW or 6kW where the batteries that RPS has on hand can power the system at up to 200kW. The benefit of power supplies in early testing is that they limit current so minor system failures will not damage expensive hardware, power supplies can limit current to less than 25 amps during a failure or mistake in the controlling software. Further as the hardware moves to the full sub-scale assembly the receiver will be wound with four turns of 1" copper strip instead of the two turns of 2" strip pictured in Fig 3.49. This is shown in Figure 3.53.
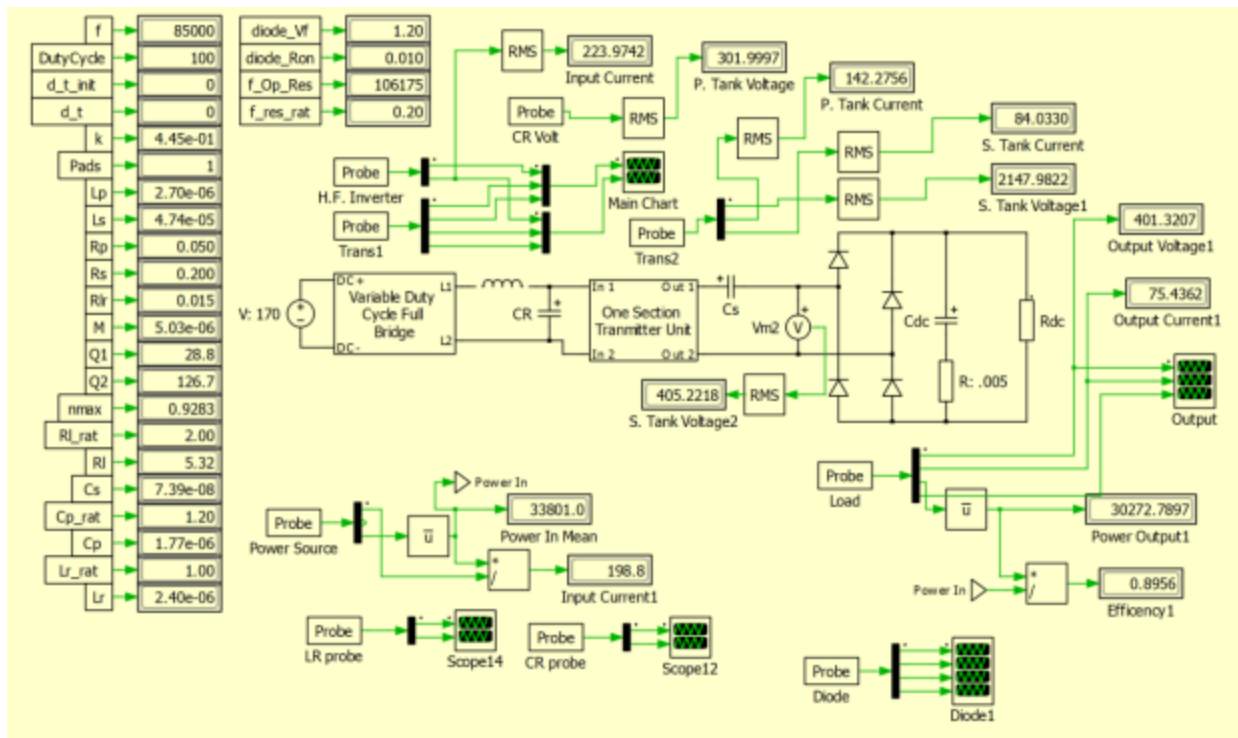
Figure 3.53 Simulation of Subscale System with 4 turn Receiver

Results of the simulation are summarized below:

- Transmitter resonating tank current of 142 amps RMS
- Transmitter resonating voltage of 301 volts RMS
- Receiver resonating tank current of 84 amps
- Receiver resonating voltage of 2147 volts
- Operating efficiency of 89.6%

This resulted in getting the efficiency close to 90% and reduced the resonating current in the transmitter coil back to under 150 amps RMS with a resonating voltage of 301 RMS. Because the multiple transmitter sections will need electromechanical contactors and exposed bus bars it is important to keep the transmitter coil resonating currents and voltages at a modest levels which they now are.

The conclusion is that a 4 turn receiver coil will be the final design and a custom high voltage series capacitor will be designed into the receiver assembly. Figure 3.54 shows the overall Subscale system test setup. The red, bule and green LED's lighted on the two printed circuit boards on the side of the stand indicate that the first 4 transmitter pads are electrically connected in series and to both legs of the high frequency AC Bus.

Figure 3.54 Static subscale system setup with 4 transmitters and 30 Volt power supplies

4. Findings and Conclusions

The inspiration of current research is to address the labor safety issue during plug-in operations of locomotive batteries. The North Carolina Department of Transportation (NCDOT) Rail Division currently owns a fleet of eight (8) F59PH and PHI diesel-electric locomotives and these locomotives are plugged into electrical ground power (480V/400A three-phase) to charge the onboard batteries. The plug-in procedure requires parking the vehicles at specific locations and the physical attachment of a heavy cable adaptor to the locomotive, which has potential of causing back pain, tripping personnel working on the tracks, and other labor safety-related risks. The project suggested the development of wireless power charging technology to replace the plug-in operations.

After the initial studies, the huge potential of the wireless power transfer technology for railway applications has been recognized and a W-I shaped coupler is developed to wirelessly charge the rail locomotives based on the current challenges and gaps of IPT technology for the railway application. The W-I shaped coupler has a relatively higher coupling coefficient and a significantly lower core volume, which can reduce the core material cost and maintain the power transfer capability. Its modular design is easy to extend to achieve a higher power rating and is compatible with static and dynamic charging.

The development involved two phases: 1) a Sub-scale system development and 2) a full-scale prototype development. The sub-scale system demonstrated charging coupling mechanisms and the prototype of the full-scale, W-I shaped coupler-base IPT system was constructed and validated at 5 kW with 92.5% efficiency, which is the highest IPT system efficiency reported for railway applications. The EMF was also measured at a reasonable test point to ensure the safety of the designed wireless charging system. All studies have been validated using numerical models developed using ANSYS Maxwell.

The full-scale prototype was demonstrated in a full-scale trailer cart that was sponsored by Belmont Trolley and the wireless power charging prototype was performed at the Belmont Public Works facility, Belmont, NC on October 12, 2022.

Finally, a separate IPT system using thin copper sheets and 4-turn receiver coil (by RPS) was presented, which shows an alternative design that is currently being customized for full-scale implementations.

5. Recommendations

Current W-I shaped coupler-based IPT system has been demonstrated at 400 V, which is compatible to the railyard plug-in charging units. However, to fully implement the WPT system at the NC DOT Railyard, it is necessary to evaluate the power electronic modifications of the existing power charging units to accommodate the IPT system. Such project should be undertaken by a commercial company.

6. Implementation and Technology Transfer Plan

The Belmont Trolley trailer cart has been recognized as an effective tool to demonstrate the WPT technology for rails to both NCDOT engineers and the public. In particular, current system can be demonstrated on temporary tracks, thus, void the necessity to coordinate with actual operational railroad routes. Hence, for technology transfer, it is recommended that NCDOT, UNC Charlotte and Belmont Trolley can coordinate joint training sessions utilizing the existing setup.

Technology Transfer: To date, the research team has demonstrated the technology at Belmont, North Carolina on October 12th, 2022. The one-day event was successfully draw in over 160 audience strong. The same event will be planned in the near future for NCDOT.

7. References

[1] Xu, Xiwen, L. Wang, K. Lin, T. Zhao, S.E. Chen, D. Cook and D. Ward, (2021) "Design Considerations of An Inductive Power Transfer System for Rail Application," 2021 IEEE Transp. Electrific. Conf. Expo (ITEC), 457-461.

[2] Kim, J.H. *et al.*, (2015) "Development of 1-MW Inductive Power Transfer System for a High-Speed Train," *IEEE Transactions on Industrial Electronics*, vol. 62, no. 10, 6242-6250.

[3] Madawala, U.K. and D.J. Thrimawithana, (2011) "A Bidirectional Inductive Power Interface for Electric Vehicles in V2G Systems," IEEE Transactions on Industrial Electronics, 58(10), 4789-4796.

[4] Li, S. and C. C. Mi, "Wireless Power Transfer for Electric Vehicle Applications," in IEEE Journal of Emerging and Selected Topics in Power Electronics, vol. 3, no. 1, pp. 4-17, March 2015.

[5] Tesla, N. (1907) "Apparatus for transmitting electrical energy.", U.S. Patent US1119732A.

[6] Lu, F., H. Zhang, C. Mi, (2017) "A Review on the Recent Development of Capacitive Wireless Power Transfer Technology.", *Energies*,10, 1752.

[7] WiT-3300 FOD System. Accessed: Jan. 1, 2020. [Online]. Available: http://www.terraelectronica.ru/pdf/WITRCITY/WiT-3300DS.pdf.

[8] WiTricity Drives EV Interoperability with New 11 kW Wireless Charging System. Accessed: Jun. 28, 2016. [Online].

[9] IPT Technology 100kW Charge Bus. [Online].

[10] Tritschler, J., S. Reichert and B. Goeldi, (2014) "A practical investigation of a high power, bidirectional charging system for electric vehicles," Proceeding, 6th Eur. Conf. Power Electron. Appl., 1-7.

[11] "ORNL Demonstrates 120-Kilowatt Wireless Charging for Vehicles." Accessed: Oct. 19, 2018. Available: https://www.ornl.gov/news/ornl-demonstrates-120- kilowatt-wireless-charging-vehicles

[12] Choi, S.Y., J. Huh, W. Y. Lee, S. W. Lee, and C.-T. Rim, (2013) "New cross-segmented power supply rails for roadway powered electric vehicles," IEEE Trans. Power Electron., 28(12), 5832–5841.

[13] Rim, C.-T. (2013) "The development and deployment of on-line electric vehicles (OLEV)," Proceedings. IEEE Energy Convers. Congr. Expo. (ECCE).

[14] Rim, C.-T (2013) "Trend of roadway powered electric vehicle technology," in Mag. Korean Inst. Power Electron., 18(4), 45–51.

[15] Huh, J., W. Y. Lee, G. H. Cho, B. H. Lee, and C.-T. Rim (2011) "Characterization of novel inductive power transfer systems for on-line electric vehicles," Proc. IEEE Appl. Power Electron. Conf. Expo. (APEC), 1975–1979.

[16] "Bombardier Begins Operation of the First Inductive High Power Charging Station for PRIMOVE Electric Buses." Accessed: Sep. 10, 2013. [Online]. Available: https://bombardier.com/en/media/news/bombardier-begins-operation-first-inductivehigh-power-charging-station-primove-electric

[17] WiT-3300 FOD System. Accessed: Nov. 1, 2017. [Online]. Available: http://www.terraelectronica.ru/pdf/WITRCITY/WiT-3300DS.pdf

[18] Schumann, P., T. Diekhans, O. Blum, U. Brenner, and A. Henkel, (2005) "Compact 7 kW inductive charging system with circular coil design," Proc. 5th Int. Electr. Drives Prod. Conf. (EDPC), Nuremberg, Germany, 2015, 1–5.

[19] NISSAN Leaf Gen. 2 – for customer, in use since Q4 of 2016. [Online]. Available: http://www.intis.de/wireless-power-transfer.html#projects

[20] Bosshard, R. and J. W. Kolar, (2016) "Multi-objective optimization of 50 kW/85 kHz IPT system for public transport," IEEE J. Emerg. Sel. Topics Power Electron., 4(4), 1370–1382.

[21] Suzuki, M. et al., (2017) "Design method for low radiated emission of 85 kHz band 44 kW rapid charger for electric bus," Proc. IEEE Appl. Power Electron. Conf. Expo. (APEC), 3695–3701.

[22] Pries, J., V. P. N. Galigekere, O. C. Onar, and G.-J. Su,(2020) "A 50-kW three-phase wireless power transfer system using bipolar windings and series resonant networks for rotating magnetic fields," IEEE Trans. Power Electron., 35(5), 4500–4517.

[23] Wave IPT—Wirelessly Charging Electric Vehicles. [Online]. Available: www.waveipt.com

[24] Ibrahim, A.U., W. Zhong and M. D. Xu, (2021) "A 50-kW Three-Channel Wireless Power Transfer System With Low Stray Magnetic Field," IEEE Trans. Power Electron., 36(9), 9941-9954.

[25] Momentum Dynamics. Accessed: Apr. 19, 2018. [Online]. Available: http://www.momentumdynamics.com

[26] Xue, L., V. Galigekere, E. Gurpinar, G. -j. Su and O. Onar, (2021) "Modular Design of Receiver Side Power Electronics for 200 kW High Power Dynamic Wireless Charging System," IEEE Transp. Electrific. Conf. & Expo (ITEC), 744-748.

[27] Covic, G.A. and J. T. Boys, (2013) "Modern Trends in Inductive Power Transfer for Transportation Applications," IEEE J. Emerg. Sel. Topics Power Electron., 1(1), 28-41.

[28] Boys, J.T., G. A. J. Elliott and G. A. Covic, (2007) "An Appropriate Magnetic Coupling Coefficient for the Design and Comparison of ICPT Pickups," IEEE Trans. Power Electron., 22(1), 333-335.

[29] Huh, J., S. Lee, C. Park, G. -H. Cho and C. -T. Rim, (2010) "High performance inductive power transfer system with narrow rail width for On-Line Electric Vehicles," IEEE Energy Conv. Congr. Expo., 647-651.

[30] Huh, J., S. W. Lee, W. Y. Lee, G. H. Cho and C. T. Rim, (2011) "Narrow-Width Inductive Power Transfer System for Online Electrical Vehicles," in IEEE Trans. Power Electron., 26(12), 3666-3679.

[31] Lee, S.K.et al., (2012) "The optimal design of high-powered power supply modules for wireless power transferred train," Elect. Syst. Aircr. Railway Ship Propulsion, 1-4.

[32] Shin, J., S. Shin, Y. Kim, S. Lee, B. Song and G. Jung, (2012) "Optimal current control of a wireless power transfer system for high power efficiency," Elect. Syst. Aircr. Railway Ship Propulsion, 1-4.

[33] Lee, C.H. et al. (2013) "Design and introduction of high power transfer system for electrical vehicles," IEEE Int. Conf. Intell. Rail Transp. Proc., 280-284.

[34] Shin, J. et al., (2014) "Design and Implementation of Shaped Magnetic-Resonance-Based Wireless Power Transfer System for Roadway-Powered Moving Electric Vehicles," IEEE Trans. Ind. Electron., 61(3), 1179-1192.

[35] Kim, J.H. et al.,(2015) "Development of 1-MW Inductive Power Transfer System for a HighSpeed Train," in IEEE Trans. Ind. Electron., 62(10), 6242-6250.

[36] Choi, S.Y., S. Y. Jeong, B. W. Gu, G. C. Lim and C. T. Rim, (2015) "Ultraslim S-Type Power Supply Rails for Roadway-Powered Electric Vehicles," in IEEE Trans. Power Electron., 30(11), 6456-6468.

[37] Lee, C.H., G. Jung, K. A. Hosani, B. Song, D. -k. Seo, D. Cho (2020) "Wireless Power Transfer System for an Autonomous Electric Vehicle," IEEE Wireless Power Transfer Conf. (WPTC), 467-470.

[38] Li, Y. et al. (2017) "Design and implementation of a novel WPT system for railway applications," IEEE PELS Workshop Emerg. Technol.: Wireless Power Transfer (WoW).

[39] Song, B., S. Cui, Y. Li, C. Zhu, (2021) "A Narrow-Rail Three-Phase Magnetic Coupler With Uniform Output Power for EV Dynamic Wireless Charging," IEEE Trans. Ind. Electron., 68(8), 6456-6469.

[40] Wang, C.S., O. H. Stielau and G. A. Covic, (2005) "Design considerations for a contactless electric vehicle battery charger," in IEEE Transactions Ind. Electron., 52(5), 1308-1314.

[41] Wang, C.S., G. A. Covic, O. H. Stielau, (2004) "Power transfer capability and bifurcation phenomena of loosely coupled inductive power transfer systems," IEEE Trans. Ind. Electron., 51(1), 148-157.

[42] Chen, Y., H. Zhang, C. -S. Shin, K. -H. Seo, S. -J. Park, D. -H. Kim, (2019) "A Comparative Study of S-S and LCC-S Compensation Topology of Inductive Power Transfer Systems for EV Chargers," IEEE 10th Int. Sym. Power Electron. Distrib. Gener. Syst. (PEDG).

[43] Zhou, Wu, Zhang and Dai, (2014) "Design and analysis of the LCL resonant convertor in inductive Power Transfer system," Int. Power Electron. Appl. Conf. Expo., Shanghai, 1271-1276.

[44] Li, W., H. Zhao, S. Li, J. Deng, T. Kan and C. C. Mi, (2015) "Integrated ${LCC} $ Compensation Topology for Wireless Charger in Electric and Plug-in Electric Vehicles," IEEE Trans. Ind. Electron., 62(7), 4215-4225.

[45] Budhia, M., G. A. Covic, J. T. Boys, C. Huang, (2011) "Development and evaluation of single sided flux couplers for contactless electric vehicle charging," IEEE Energy Conv. Congr. Expo., 614-621.

[46] International Commission on Non-Ionizing Radiation Protection, (2010) "Guidelines for limiting exposure to time-varying electric and magnetic fields (1 Hz to 100 kHz)," Health Physics, 99(6), 818–836.

[47] IEEE Standard for Safety Levels with Respect to Human Exposure to Radio Frequency Electromagnetic Fields, 3 kHz to 300 GHz, IEEE C95.1-2005. [Online].

[48] Electric vehicle wireless power transfer (WPT) systems, IEC TS 61980. [Online]. Available: https://webstore.iec.ch/searchform&q=IEC%20TS%2061980

[49] Wang, Y., H. Wang, T. Liang, X. Zhang, D. Xu and L. Cai, (2017) "Analysis and design of an LCC/S compensated resonant converter for inductively coupled power transfer," IEEE Transp. Electrific. Conf. and Expo, Asia-Pacific (ITEC Asia-Pacific).

[50] DigiKey Electronics - Electronic Components Distributor, www.digikey.com/products/en?keywords=1779-1059-ND

[51] Aydin, E., Y. Kosesoy, E. Yildiriz and M. Timur Aydemir, (2018) "Comparison of Hexagonal and Square Coils for Use in Wireless Charging of Electric Vehicle Battery," International Symposium on Electronics and Telecommunications (ISETC), Timisoara, 1-4.

[52] Kosesoy, Y., E. Aydin, E. Yildiriz and M. T. Aydemir, (2019) "Design and Implementation of a 1-kW Wireless Power Transfer System for EV Charging," IEEE 13th International Conf. Compatibility, Power Electronics and Power Engineering (CPE-POWERENG), Sonderborg, Denmark, 1-5.

[53] Jayalath, S., A. Khan, (2018) "Analysis of the Relationship between the Parameters of IPT Transformer and Power Electronic System," IEEE Wireless Power Transfer Conf. (WPTC), Montreal, QC, 1-4.

[54] Tan, P., F. Yi, C. Liu and Y. Guo, (2018) "Modeling of Mutual Inductance for Hexagonal Coils with Horizontal Misalignment in Wireless Power Transfer," IEEE Energy Conversion Congress and Exposition (ECCE), Portland, OR, 1981-1986.

[55] Sampath, J.P.K., A. Alphones, D.M. Vilathgamuwa, A. Ong and X.B. Nguyen, (2014) "Coil enhancements for high efficiency wireless power transfer applications," IECON, 40th Conference IEEE Industrial Electronics Society, Dallas, TX, 2978-2983.

[56] Khan, S.R., S. K. Pavuluri and M. P. Y. Desmulliez (2018) "Accurate Modeling of Coil Inductance for Near-Field Wireless Power Transfer," IEEE Trans. Microwave Theory and Techniques, 66(9), 4158-4169.

[57] Liu, Z., Z. Chen, J. Li and H. Zhao (2018) "A Shape-Reconfigurable Modularized Wireless Power Transfer Array System for Multipurpose Wireless Charging Applications," in IEEE Transactions on Antennas and Propagation, 66(8), 4252-4259.

[58] Khan, S.R., S. K. Pavuluri and M. P. Y. Desmulliez (2018) "New analytical model for the characterisation of printed spiral coils for wireless power transfer," 12th European Conf. Antennas and Propagation (EuCAP 2018), London, 1-5.

[59] Melki, R., B. Moslem, (2015) "Optimizing the design parameters of a wireless power transfer system for maximizing power transfer efficiency: A simulation study," Third Int. Conf. Technological Advances in Electrical, Electronics and Computer Engineering (TAEECE), Beirut, 278-282.

[60] Wang, L., T. Zhao, S. -E. Chen and D. Cook, "An Inductive Power Transfer System Design for Rail Applications," in 2018 IEEE Trans. Electrific. Conf. Expo (ITEC), 2018, pp. 84-89

[61] Carpenter, D.O. (2013) "Human disease resulting from exposure to electromagnetic fields," Rev Environ Health, 28(4):159-72.

[62] Campi, T., S. Cruciani, V. De Santis and M. Feliziani, (2016) "EMF Safety and Thermal Aspects in a Pacemaker Equipped with a Wireless Power Transfer System Working at Low Frequency," *IEEE Transactions on Microwave Theory and Techniques*, 64(2), 375-382.

[63] International Commission on Non-Ionizing Radiation Protection, (2010) "Guidelines for Limiting Exposure to Time-Varying Electric and Magnetic Fields (1 Hz to 100 kHz)," Health Phys., 99(6), 818-836.

[64] "Wireless Power Transfer for Light-Duty Plug-in/Electric Vehicles and Alignment Methodology," J2954_202010. [Online]. Available: https://www.sae.org/standards/content/j2954_202010

[65] BS-IEC-62957-1 › Radiation protection instrumentation. Semi-empirical method for performance evaluation of detection and radionuclide identification